Operation and Performance of a Magnetically Shielded Hall Thruster at Ultrahigh Current Densities on Xenon and Krypton

Leanne L. Su*, Tate M. Gill*, Parker J. Roberts*, William J. Hurley*, Thomas A. Marks*, Christopher L. Sercel*, Madison G. Allen*, Collin B. Whittaker*, Matthew P. Byrne[†], Zachariah B. Brown*, Eric Viges[‡], and Benjamin A. Jorns[§]

University of Michigan, Ann Arbor, MI, 48109

The performance of a 9-kW class magnetically shielded Hall thruster is characterized at 300 V discharge voltage for a channel current density a factor of ten greater than the nominal current density associated with its 300 V and 4.5 kW condition. An inverted pendulum thrust stand and a far-field probe suite are employed to measure the global performance and efficiency modes respectively. It is found that when operating on xenon, thruster anode efficiencies range from 52.9 ±0.8% to 62.2 ±2.2% over the power range of 4.5–37.5 kW at 300 V. Anode efficiencies for krypton span from 48.5 ±7.0% to 56.4 ±1.0% at 4.5–45 kW at 300 V. The thrust and specific impulse are found to be 1650 ±10 mN and 2309 ±17 s respectively at 37.5 kW for xenon and 1839 ±10 mN and 2567 ±16 s for 45 kW on krypton. The thrust density at the maximum power setting of 45 kW is shown to be ~7× higher than its nominal 4.5 kW condition. It is also demonstrated that the thruster can achieve thrust densities and thrust-to-power ratios on par with or even greater than applied-field magnetoplasmadynamic thrusters in the sub-50 kW power range. These results are discussed in the context of Hall thruster theory, conventional scaling laws for the maximum achievable current density in these devices, and challenges with high power thruster testing. The implications of the demonstrated ability to achieve atypically high current densities with minimal performance reduction for high power electric propulsion development are also examined.

Nomenclature

δ	Uncertainty in thrust stand parameter
$\dot{m}_a$	Anode neutral mass flow
$\dot{m}_b$	Beam ion mass flow
$\dot{m}_{fac}$	Facility mass flow rate
η_b	Beam current utilization efficiency
η_b	Mass utilization efficiency
η_d	Plume divergence efficiency
η_q	Charge utilization efficiency
η_v	Voltage utilization efficiency
$\eta_{a,probe}$	Anode efficiency as measured by probe suite
$\eta_{a,thrust}$	Anode efficiency as measured by thrust stand
η_{fac}	Facility correctional efficiency
η_{tot}	Total efficiency
γ_i	i^{th} secondary electron emission coefficient
κ_G	Probe correctional factor
κ_{SEE}	Secondary electron emission correctional factor
λ_{iz}	Ionization mean free path
Ω_i	i^{th} current fraction
ϕ_f	Floating potential
ϕ_p	Plasma potential

---

*Ph.D. Candidate, Department of Aerospace Engineering, AIAA Student Member
[†]Ph.D. Candidate, Department of Applied Physics, AIAA Student Member
[‡]Senior Research Engineer, College of Engineering
[§]Associate Professor, Department of Aerospace Engineering, AIAA Associate Fellow

σ_{iz}	Ionization cross-section
θ_d	Plume divergence angle
A_C	Collector area
b	y-intercept of thrust stand calibration curve
d	Density of material deposited on QCM
D_T	H9 thruster diameter
e	Elementary charge
f	QCM thickness
F_T	Thrust force
g_0	Gravitational constant
h_C	Collector height
h_{GR}	Guard ring height
I_b	Beam current
I_d	Discharge current
I_{FP}	Current collected by Faraday probe
$I_{N,off}$	Thrust stand null coil current after shutdown
$I_{N,on}$	Thrust stand null coil current before shutdown
I_{sp}	Total specific impulse
j	Current density
K	QCM constant factor
m	Slope of thrust stand calibration curve
m_e	Electron mass
m_i	Ion mass
N	Number of samples in thrust averaging window
n_i	Ion density
n_n	Neutral density
P_d	Discharge power
R	Probe suite measurement radius
R_C	Collector radius
R_{GR}	Guard ring radius
T	Thrust
t	QCM deposition thickness
T_e	Electron temperature
V_a	Acceleration voltage
V_d	Discharge voltage
v_e	Thermal electron velocity
V_{RPA}	Voltage measured by RPA
Z_i	i^{th} charge state
Z_{avg}	Effective average charge state

I. Introduction

The development of high-power (>100 kW), lightweight, and high-performance electric propulsion (EP) technologies is critical for enabling the next generation of deep-space crewed missions. As outlined in the recent NASA-commissioned study by the National Academy of Engineering (NAE) on nuclear-powered missions to Mars, baseline requirements for future EP systems include input powers greater than 2 MW, specific impulse exceeding 2000 s, efficiency greater than 50% and system specific mass less than 5 kg/kW [1]. While there are a number of technologies proposed to meet these requirements [1, 2], the Hall effect thruster is a particularly promising candidate that has been featured in recent trades on NASA's proposed nuclear electric propulsion plan for Mars [3]. Indeed, this thruster class has extensive development and flight heritage at power levels below 12.5 kW [4–9], and laboratory models have been demonstrated up to 100 kW [10–13]. Hall thrusters have also been shown to be generally capable of meeting the specific impulse, efficiency, and specific mass requirements for near-term nuclear architecture [1, 3].

Despite these attractive capabilities, thrust density remains a major limitation of this technology in the context of high-power applications. Historically, Hall thruster design has followed generalized scaling laws [14–16], including

the requirement that the "optimum" current density in the channel is 100–150 mA/cm^2 [16]. As a direct result, the thrust density of most Hall thrusters has been limited to 10 N/m^2 [17]. This metric can be an order of magnitude higher than other technologies like gridded ion thrusters, which makes Hall thrusters attractive for mid-power applications. However, for the 100 kW–1 MW levels envisioned for nuclear architectures, Hall thruster size can become prohibitively large. It is in part for this reason that magnetoplasmadynamic thrusters (MPD) with their inherently high thrust density have historically been the baseline option for high power operation [3].

Faced with this limitation, the NAE study had a recommendation to explore methods for increasing thrust densities of Hall thrusters. This can be accomplished, for example, by increasing the acceleration voltage (and therefore specific impulse) while still maintaining the optimum level of current density [16]. The TSNIIMASH laboratory DL-160 thruster [13] with active water cooling followed this approach, demonstrating 140 kW at 8 kV discharge voltage on bismuth with a thruster efficiency greater than 70%. Assuming a 160 mm diameter channel, this yielded an approximate thrust density over 100 N/m^2—an order of magnitude higher than the typical thrust density of a Hall thruster at 300 V [17]. With that said, the specific impulse on this system approached 8000 s and thus a thrust-to-power ratio that was likely too low for a crewed Mars architectures.

As an alternative solution, nested Hall thrusters with concentrically stacked channels have been proposed for increasing thrust density and reducing specific mass [10, 18]. Even in the ideal limit, however, where the nesting is so close that the entire thruster surface effectively generates thrust, the increase in thrust density over a single channel is only a factor of two. To this point, for the approximate dimensions (c.f.[11]) of the 100-kW X3 nested thruster tested under the NASA NextSTEP program, the thrust density was the same as the nominal 10 N/m^2 typical of single channel thrusters. In summary, attempts to increase thrust density to date have resulted in prohibitively high specific impulse or only marginal improvement. These limitations ultimately stem from the fact that the proposed solutions were designed to try to increase thrust density while respecting the design rule for nominal current density.

There is reason to believe, however, that this limit on maximum current density may not be absolute. It has been suggested that rather than being entirely-physics based, this conventional design rule may simply be a consequence of modern designs being informed by heritage from a common predecessor [14]. More fundamentally, a common justification for this limit is that increasing current density leads to a degradation in performance due to a loss in electron confinement. However, this argument is based on the assumption that the electron confinement in Hall thrusters is classical, whereas in practice, the electron dynamics are driven by non-classical effects [19]. To this point, Simmonds et al. recently performed a theoretical study of the thrust density in Hall thrusters allowing for non-classical transport [17]. These authors ultimately concluded that the theoretical limit on thrust density is several orders of magnitude higher than the currently accepted rule of thumb. We in turn recently established in a study of a laboratory magnetically shielded thruster that we were able to increase the current density by a factor of 2.7 from nominal without a loss in performance [20]. In light of these theoretical arguments, previous exploratory studies, and the major advantages of being able to operate Hall thrusters at higher current density, the need is apparent for an expanded and detailed experimental study on the impact of increased current density on Hall thruster operation. This is the primary goal of this study.

As a secondary consideration, we note that even if we can establish the ability to operate at higher power and thrust density, there remain major technical obstacles in the testing of any high power Hall thruster in ground-based facilities. Examples include the influence of background pressure on thruster performance and stability [21], thermal loading on the facility [22], and backsputter rates that can obscure the results of wear tests [23]. It is with these challenges in mind that the NASA Space Technology Research Institute, the Joint Advanced Propulsion Institute (JANUS), was recently formed to study the problem of ground testing for higher power concepts [24]. A major challenge, however, for investigating facility effects at high power is that our experience at these power levels is limited: cumulative testing time across the entire community above 100 kW for Hall thrusters is on the order of minutes to hours. An additional goal of this effort therefore is to expand the dataset of testing issues that may be encountered at higher power and high power density. These insights will inform follow-on work at JANUS.

With these two objectives in mind—to investigate fundamental limits of current density in Hall thrusters and to characterize facility effects at higher power operation—this work is organized in the following way. In Sec. II, we overview the experimental setup including the test article, facility, and test points. In Sec. III, we describe the methodology for characterizing our thruster's performance. In Sec. IV, we overview the diagnostics and analysis methods. In Sec. V, we present the key results of our study. Finally, in Sec. VI, we discuss explanations for our findings and their implications for our understanding of Hall thruster operation.

II. Experimental Setup

We describe in this section the experimental setup for this test campaign. We first overview the 9-kW class test article and the modifications we employed to adapt it for testing at increased power density. We then describe the test facility where we performed this campaign and the operating conditions for the thruster.

A. Test article

We employed a modified version of the H9 Hall effect thruster for this study known as the "H9 MUSCLE" (Fig. 1). The baseline 9-kW laboratory device was designed by the Jet Propulsion Laboratory (JPL) in collaboration with the University of Michigan and the Air Force Research Laboratory [25, 26]. It is intended to serve as a common platform for shared research, a vehicle for investigation into new innovations in Hall thruster technology and physics, and a training instrument for the education of the next generation of scientists in the field.

As described in Refs. [25–27], the H9 has a stainless steel anode, graphite pole covers on the magnetic circuit, and a centrally-mounted LaB$_6$ cathode with graphite keeper. The H9 also employs a 'magnetically shielded' field topology, a method that shapes field contours to establish a potential gradient directed away from the channel walls [28, 29]. This serves in part to help isolate the chamber from the main discharge while also accelerating energetic ions away from the channel walls. This technique has been shown to improve the lifetime of Hall thrusters by an order of magnitude over non-shielded thrusters with only a minor (<2%) decrease to its efficiency [29].

The H9 has been the subject of a series of performance measurements and basic plasma measurements [20, 25–27, 30] and has been experimentally characterized on both xenon and krypton. The nominal operating envelope of the H9 on xenon is approximately 4.5–12 kW discharge power, 1800-3000 s specific impulse, and 290–700 mN thrust. Typical total efficiency values over this operating envelope range from 55-70%. The operating envelope on krypton is from 4.5–9 kW discharge power, 1900–2700 s specific impulse, 260–350 mN thrust, and 45-55% anode efficiency.

(a)   **(b)**
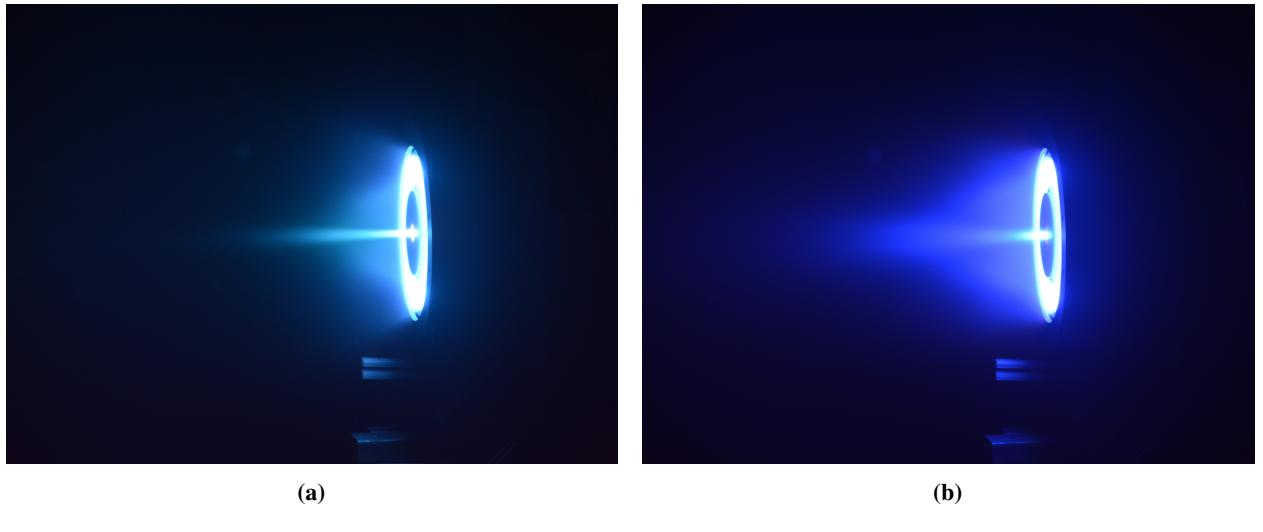
Fig. 1   a) Modified H9 MUSCLE operating in the Large Vacuum Test Facility operating on xenon at 300 V discharge voltage and 125 A discharge current and b) on krypton at 300 V and 150 A.

We made two major modifications to the H9 to facilitate our investigation into high current density operation. First, we replaced the baseline boron nitride channel with an entirely graphite discharge chamber. This modification was previously demonstrated with the H9C, a graphite-walled version of the H9 characterized by JPL [27]. The adoption of graphite is largely enabled by the magnetically shielded topology, which serves to help mitigate the wall losses traditionally incurred by using non-insulating materials for the walls of unshielded thrusters [27, 31, 32]. For our study, graphite has the advantage of being more thermally emissive and conductive as well as more resilient to thermal shock than boron nitride. It is because of these properties that this material previously has been suggested as being particularly suited for high power density modes of operation [27]. The graphite chamber was held at anode potential and isolated from the thruster body during operation.

For our second modification to the H9, we implemented an active water-cooling loop for the magnetic circuit. This non-flightlike change alleviated thermal issues related to enhanced plasma flux to the channel walls at high

current density. It thus allowed us to focus on the more fundamental question of the role of current density on thruster performance. A similar modification for cooling has been applied in previous laboratory experiments of high power Hall thruster operation [13].

B. Facility

The test was conducted in the Large Vacuum Test Facility (LVTF) at the University of Michigan, a 6 m diameter by 9 m long vacuum chamber with a nominal pumping capacity of 500 kL/s for xenon and 600 kL/s for krypton [33]. A top-down view of the chamber and experimental setup is shown in Fig. 2. In this configuration, the thruster is mounted on the centerline of the chamber and directed toward a downstream probe suite (Sec .IV.B). A Faraday probe and camera, aligned vertically to thruster centerline, allows for azimuthal sweeps at a constant radius with respect to the thruster. During operation, the thruster fires downstream into a chevroned graphite beam dump that is held at facility potential. The graphite backsputter in the plane of the thruster in turn is monitored with a QCM (Sec. IV.G).

A xenon-calibrated Stabil ion gauge with a stainless steel neutralizer tube with grounded metal mesh was mounted 1 m away from the thruster in the exit plane [34]. When operating the thruster on krypton, we applied a correction of 1.48 to gauge readings, per the manufacturer guidelines. We note here that although this gauge's calibration was recent, its reported pressures appeared to be about a factor of 1.8 low when compared to conditions previously reported at similar operating conditions on the H9 [20, 30]. Absent an independent pressure measurement during this campaign, we were unable to directly discount the validity of these measurements. However, we proceed in the following analysis with the assumption that our values may underreport facility pressure by a factor of 1.8. This uncertainty is reflected in the corrections we make in our analysis that are related to the facility environment.
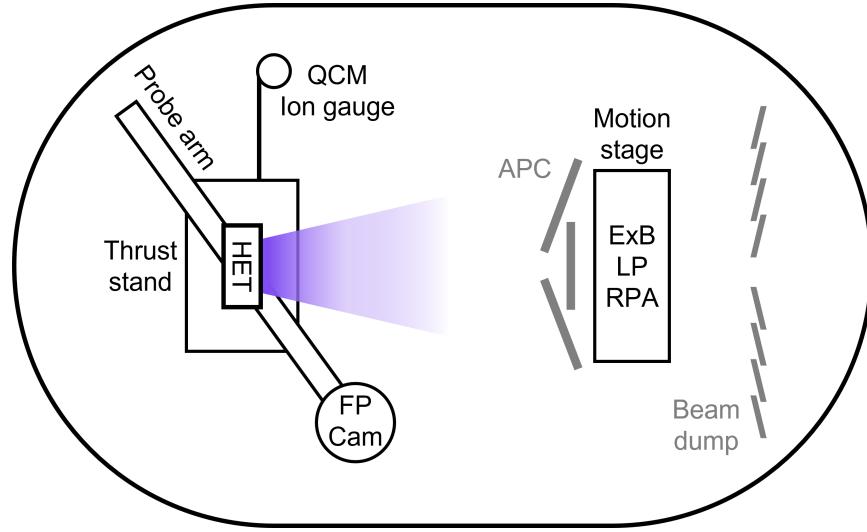

Fig. 2   Notional top-down schematic of experimental setup in LVTF, including thruster, ion gauge, armored probe carrier with E×B probe, Langmuir probe, and RPA, probe arm with Faraday probe and camera, and beam dump. Pumps are located around the walls of the facility but not shown in the diagram.

We employed an Alicat MC-series 3000 sccm mass flow controller for anode flow and a 400 sccm mass flow controller for cathode flow. Both of these flow controllers have a measurement error of ±0.1% of full scale and were calibrated independently for xenon and krypton with a MesaLabs Bios DryCal Definer 220 flow calibration unit. We used a Magna-Power Electronics 150-kW power supply rated to 1000 V and 150 A to supply discharge power to the thruster and a series of Lambda TDK DC power supplies for the magnets and cathode keeper/heater. The return from the discharge power was passed through a filter circuit with a 0.3 mH inductor, 47 μF capacitor, and 10 Ω resistor to protect the power supply from oscillations in the thruster current.

C. Operating conditions and configuration

Table 1 shows the operating conditions we experimentally characterized in this campaign. We operated the thruster at a constant discharge voltage of 300 V for all points and varied the anode flow rate until achieving the target discharge

current. The cathode flow fraction was held at 7% for all operating conditions, and we employed a magnetic field strength of 112.5% its nominal value for this thruster. The thruster body was electrically tied to facility ground, a necessary configuration resulting from the cooling system we employed. As a general approach, we progressively increased thruster power during the test campaign by increasing the flow to control current. At each new operating condition, we waited until the thruster mean discharge current achieved a constant value before performing a far-field probe sweep. We then shut down the thruster to generate a zero point for a thruster measurement. Finally, we restarted the thruster and rapidly ramped up to the next operating condition. This process typically resulted in a 5–15 minute dwell time at each operating point. While we attempted to visit the same discharge current conditions for both gases, we were unable to reach the 150 A condition for xenon due to a later-resolved issue in the electrical harnessing.

Current (A)	Power (kW)	Xe $\dot{m}_a$ (sccm, mg/s)	Xe pressure (μtorr-Xe)	Kr $\dot{m}_a$ (sccm, mg/s)	Kr pressure (μtorr-Kr)
15	4.5	169, 15.2	2.6	196, 11.2	2.7
50	15	400, 35.9	5.6	537, 30.7	6.6
75	22.5	519, 46.7	7.5	726, 41.5	8.8
100	30	644, 57.9	9.2	885, 50.6	10.8
125	37.5	757, 68.1	10.7	1040, 59.5	12.8
150	45	-	-	1193, 68.3	14.4

Table 1   Operating conditions for test points characterized during this effort. The discharge voltage was 300 V for all conditions. Note that the listed pressures are uncorrected for the 1.8× discrepancy.

III. Methodology for Characterizing Performance

In this section, we describe the framework we employed to evaluate the performance of this Hall thruster. We briefly overview key global parameters such as thrust, specific impulse, and anode efficiency, as well as definitions for the constituent efficiency modes for the thruster.

A. Global performance metrics

The primary measurement we employed for determining global performance metrics for our thruster is thrust, T, a measure of the total force. From thrust, we can determine specific impulse:

$$I_{sp} = \frac{T}{\dot{m}g_0}, \tag{1}$$

where $\dot{m}$ is the total mass flow rate and g_0 is the gravitational acceleration. We also define the total electrical efficiency:

$$\eta_{tot} = \frac{T^2}{2\dot{m}P}, \tag{2}$$

where the total mass flow is combined from the anode and cathode, $\dot{m} = \dot{m}_a + \dot{m}_c$, and the total power is the summation of discharge and magnet power, $P = P_d + P_{mag}$. The discharge power is calculated from $P_d = V_d I_d$, where I_d is discharge current and V_d is discharge voltage. The electrical efficiency indicates the fraction of total power converted to useful kinetic energy for thrust generation.

In order to characterize the operation exclusively for the channel without the effect of losses from the magnets and cathode, we also introduce the anode efficiency:

$$\eta_a = \frac{T^2}{2\dot{m}_a P_d}. \tag{3}$$

We note here that for the high facility background pressures we found in this work, neutral ingestion can act as an additional source of propellant flow into the channel, $\dot{m}_{fac}$. This can artificially raise estimates for the thruster efficiency. To correct for this, we follow Refs. [10, 35] in defining a facility correction factor:

$$\eta_{fac} = \frac{\dot{m}_a}{\dot{m}_a + \dot{m}_{fac}}. \tag{4}$$

6

This correction is applied to calculations of the anode efficiency and total efficiency. To determine the effective facility neutral ingestion for our setup, we employed the model motivated in Ref. [35] updated for the pump configuration in LVTF [33]. In practice, we found the average facility neutral ingestion to contribute less than a 0.5% correction to measured efficiencies.

B. Efficiency modes

The anode efficiency can be broken down into various non-ideal processes within the Hall thruster. We quantify five partial efficiencies following the Hall thruster model developed by Hofer et al. [16, 36–38]:

$$\eta_a = \eta_b \eta_q \eta_m \eta_v \eta_d. \tag{5}$$

Here η_b is the beam current utilization efficiency, η_q is the charge utilization efficiency, η_m is the mass utilization efficiency, η_v is the voltage utilization efficiency, and η_d is the plume divergence efficiency. We can use this model to identify how specific processes within the thruster are contributing to performance losses. We describe the physical significance of each of these efficiency modes in this section.

Beam current utilization efficiency: the ratio of ion current in the plume to the discharge current is defined as

$$\eta_b = \frac{I_b}{I_d}, \tag{6}$$

where I_b is the ion beam current. This metric captures the fact that not all of the discharge current is carried by ions, as some is carried by electrons from the cathode to the anode. Lower values of beam utilization efficiency correspond to reduced electron confinement in the thruster channel. This efficiency is believed to be a major driver for degraded performance at higher current density.

Charge utilization efficiency: the decrease in efficiency from multiply-charged ions in the beam is defined as

$$\eta_q = \frac{\left(\sum_i \frac{\Omega_i}{\sqrt{Z_i}} \right)^2}{\sum_i \frac{\Omega_i}{Z_i}}, \tag{7}$$

where Z_i is the charge state of the ith ion species, $\Omega_i = \frac{I_i}{I_d}$ is the current fraction of the ith ion species, and I_i is the total contribution to current from a given ion species. This efficiency encapsulates the fact that the plume is not monoenergetic.

Mass utilization efficiency: the ratio of beam ion mass flux to neutral mass flux through the anode is defined as

$$\eta_m = \frac{\dot{m}_b}{\dot{m}_a} = \frac{\frac{m_i I_b}{e} \sum_i \frac{\Omega_i}{Z_i}}{\dot{m}_a} = \xi \eta_b \sum_i \frac{\Omega_i}{Z_i}, \tag{8}$$

where $\dot{m}_a$ is the neutral anode mass flow rate, $\dot{m}_b$ is the ion beam mass flow rate, m_i is the ion mass, e is the elementary charge, and $\xi = \frac{I_d m_i}{e \dot{m}_a}$ is a value defined as the exchange ratio. This efficiency loss is due to the fact that not all neutrals are ionized and accelerated out of the channel, therefore not contributing to thrust.

Voltage utilization efficiency: the conversion of applied voltage into ion velocity is defined as

$$\eta_v = \frac{V_a}{V_d}, \tag{9}$$

where V_a is the average acceleration voltage, the potential drop through which ions are accelerated in the channel. This efficiency represents the loss in discharge voltage that is not available for accelerating ions. This factor is decreased when ions are born downstream of the peak potential and when the voltage required to extract electrons from the cathode increases.

Plume divergence efficiency: the ratio of radially-directed to axially-directed momentum in the beam is defined as

$$\eta_d = (\cos\theta_d)^2, \tag{10}$$

where θ_d is the divergence angle of the beam as measured from channel centerline. This efficiency captures the fact that only axially-directed momentum imparts thrust.

Armed with these definitions for performance and efficiency, we describe in the next section our experimental methods for characterizing these properties.

IV. Diagnostics

In this section, we describe the diagnostics we used to characterize the thruster performance and health. We begin with a description of the thrust stand we employed to measure the global performance. We then describe the far-field probes we used to measure the various efficiency modes. We conclude with an overview of the diagnostics for characterizing thruster and facility health.

A. Thrust stand

We employed for this campaign an inverted pendulum thrust stand [22] with spring flexures that provided a restoring force against the thruster weight. The thrust stand assembly, shown in Fig. 3, was surrounded by a radiative shroud, which was maintained at a temperature of 20° C by a chiller pump to reduce thermal drifts. We operated the thrust stand in a null displacement mode by actively controlling the position with a null coil solenoid and plunger. Displacement was monitored with a fiber-optic sensor, while an analog PID controller provided the control signal for the solenoid. We also maintained constant thruster pitch inclination via a stepper motor with software-based control. With this approach, we took a thrust point by recording the difference in solenoid current before after shutting down the thruster, $I_{N,on}$ and $I_{N,off}$ respectively. During this shutdown process, we eliminated the impact of cold gas contributions to thrust by cutting off gas flow with software-actuated solenoid valves.
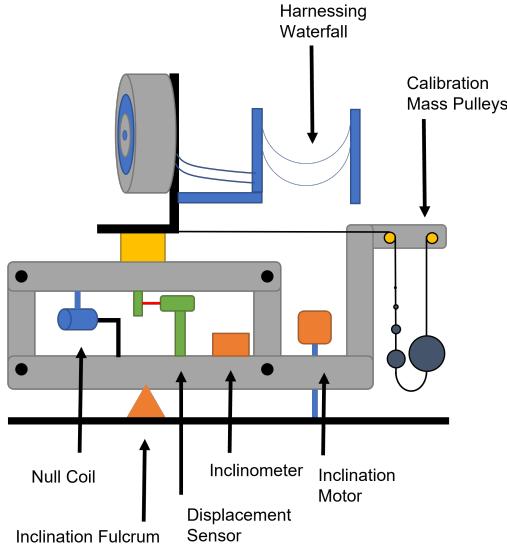

Fig. 3   Schematic of the null-displacement force balance used to measure thrust.

We calibrated the thrust stand with a series of known masses corresponding to thrusts ranging from 10 mN to 4.8 N. Fig. 4 shows an example result of this calibration process where we have fit a curve of the form $\Delta I_N = mF_T + b$. Here, ΔI_N is the change in null coil current, F_T is the thrust (or calibration weight) force, and m and b are the slope and intercept of the line of best fit. When performing measurements, we inverted this expression to determine the thrust as a function of the coil current during thruster operation: $F_T = \left(\left[I_{N,on} - I_{N,off}\right] - b\right)/m$.

We quantified uncertainty in our thrust measurements as

$$\delta F_T^2 = \frac{\delta I_{N,on}^2 + \delta I_{N,off}^2 + \delta b^2 + F_T^2 \delta m^2}{m^2}. \tag{11}$$

Here $\delta I_{N,on}, \delta I_{N,off}$ represent the variance in the null coil currents and $\delta m, \delta b$ denote uncertainty from the slope and offset of the least-squares fit to the calibration curve. These latter factors incorporate any random variation in the repeatability of thrust values during the calibration process. We found uncertainties in thrust ranging from 8–17 mN across all operating conditions. We note here that thermal drifts at high-power-density operating conditions did result in systematic trends in the thrust curve as a function of time. However, we chose current measurement windows close enough to the shutdown point that the timescale of these thermally-induced drifts could be ignored.

(a)   (b)
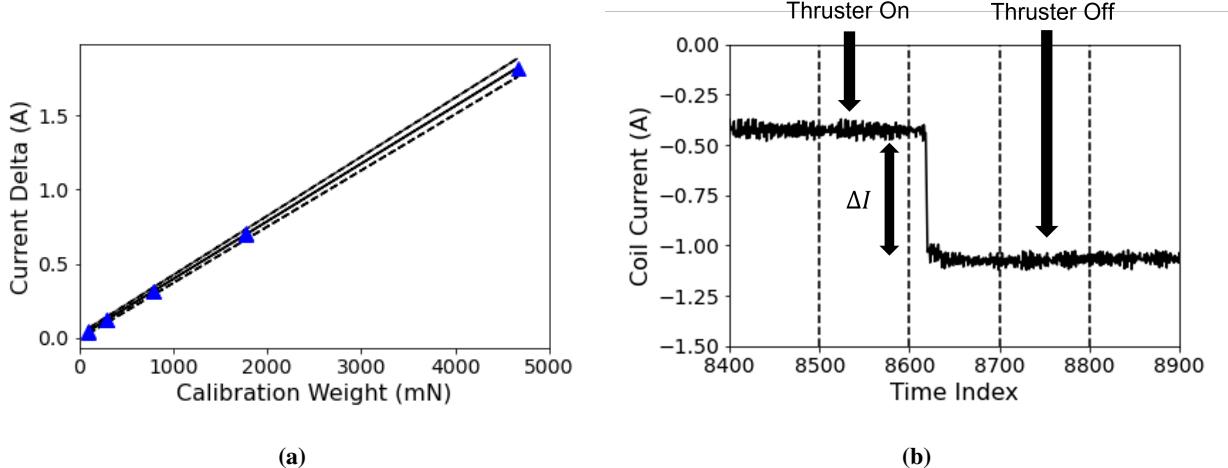
Fig. 4   a) An example thrust calibration curve with 10σ uncertainty bounds shown. In practice, the credible interval is much narrower than the best-fit line. b) An example thrust point taken by shutting the thruster off and monitoring the change in null coil current.

B. Far field probe shield

We employed a standard set of far-field probes for this experimental effort including a swept Faraday probe, retarding potential analyzer, E×B probe, and Langmuir probe (Fig. 5b). With the exception of the Faraday probe, which was mounted on an azimuthally swept arm, these probes were located ∼14 D_T downstream of the thruster along thruster centerline. As our goal was to investigate thruster performance at abnormally high current densities, we anticipated that thermal loading and erosion may pose a challenge for the protection of these probes. To attempt to mitigate these issues, we implemented a probe shield, the Armored Probe Carrier (APC) (Fig. 5a), which consisted of a linear motion stage shielded by three large graphite plates. Each probe in turn was mounted at a different linear position on this translation stage. The shields were stood off from the main structure of the APC with stainless steel washers to provide thermal isolation and prevent the motion stage from overheating at high beam powers. A small cutout was located in the central graphite shield, set between the two angled panels, and aligned to thruster channel centerline at 3 o'clock. When not actively using one of the probes located on the APC, the suite was in the 'rest' position where all probes were fully shielded by the graphite panels. During each probing phase, each probe was translated to the appropriate location such that it had a line of sight to the thruster channel through the cutout.

C. Retarding potential analyzer

A retarding potential analyzer (RPA) is a gridded electrode plasma diagnostic used to measure the ion energy distribution function (IEDF) of a plasma along the probe axis. These measurements, which are related to the average ion energy, inform the calculation of voltage utilization efficiency (Eq. 9). During operation, a quasineutral plasma enters the aperture and passes through the first grid, which floats to plasma potential. The second grid is the primary electron suppression grid, which is biased negatively to prevent electrons from passing through it. The third grid is the
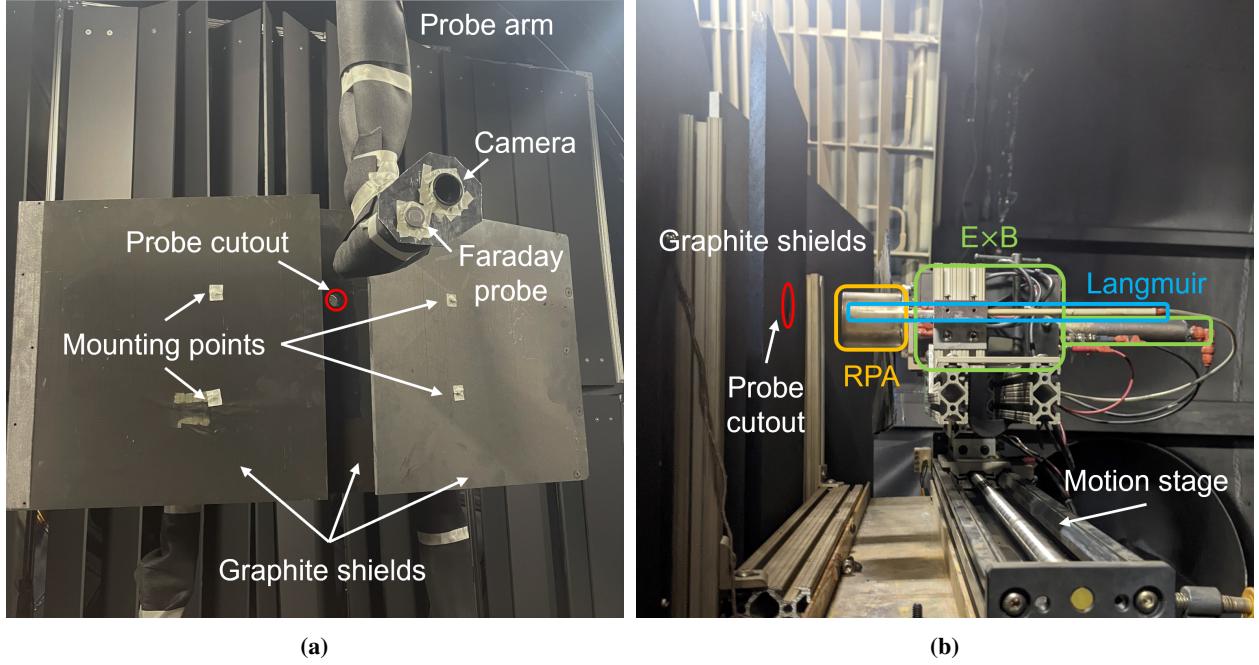
Fig. 5 Photos of probe setup inside the vacuum facility showing a a) front view of the APC and probe arm, and b) side view of the APC. The side view shows the three probes (from nearest to furthest: Langmuir, RPA, E×B) mounted on the motion stage behind the graphite panels.

ion selector grid, which is biased to a user-controlled potential V_{bias}. Ions with energies above V_{bias} are able to pass through the grid, while those with lower energies are repelled. The final grid is the secondary electron suppression grid, biased to the same potential as the other electron suppression grid, which prevents secondary electrons created inside the probe from reaching the collector. This process ensures that only ion current was collected. We employed an RPA with an aperture area of 6.45 cm^2 and four grids in front of a current collector. Both electron suppression grids were biased to -30 V.
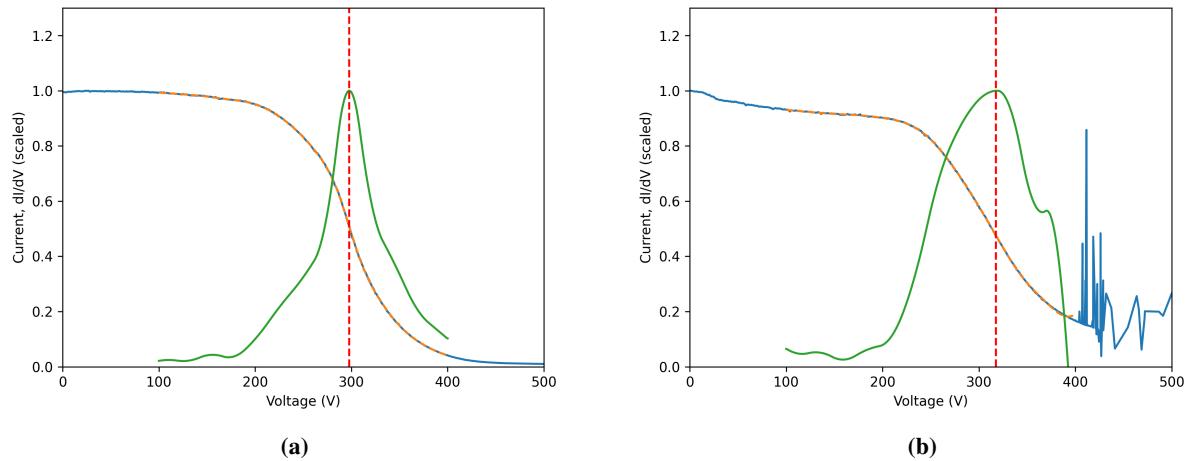

Fig. 6 RPA data for xenon at a) 300 V and 15 A and b) 300 V and 125 A. The original data are shown in blue, a smoothing spline fit is shown as a yellow dashed line on top of the original data, the IEDF is shown in green, and the location of the most probable voltage is depicted as a vertical red dashed line.

The ion selection grid voltage V_{bias} was swept from 0 to 500 V during this effort. At 0 V, all ions from the plasma were able to make it to the collector, while at 500 V, effectively no ions were able to reach the collector. This was dictated by the fact that our discharge voltage was maintained at 300 V during this campaign. We diferentiate the current collected as a function of voltage to yield an estimate of the IEDF (expressed as a function of energy per unit charge). The location of the peak of the IEDF corresponds to the most probable ion voltage referenced with respect to ground. We in turn use this quantity corrected by measurements of the local plasma potential (see next section) to determine the average ion energy V_a. This informs our estimates for the voltage utilization efficiency (Eq. 9).

In Fig. 6, we show example RPA traces, along with smoothing spline fits, computed IEDFs, and estimated most probable voltages. We employed bootstrapping to estimate the error in the most probable voltage by sampling a subset of the raw RPA trace and performing the same method as described above for determining the most probable voltage [39]. This process was repeated 1000 times, and 2× the standard deviation in the resultant values of most probable voltage was taken to be the uncertainty.

We note here that for high discharge currents at ion selector voltages above 400 V in Fig. 6b, the RPA trace exhibited marked noise in the signal. We believe this was due to the increasingly high current density in the diagnostic at these operating conditions, leading to internal arcing of the grids. As this probe was originally designed for standard Hall thruster operating conditions, this type of breakdown at high current densities was not anticipated. It does suggest, however, that additional consideration should be given to design of diagnostics for this operational regime. We return to this point in Sec. VI.D.

D. Langmuir probe

The Langmuir probe (LP) we used consisted of a 1 mm diameter by 4 mm length of tungsten wire extending past an alumina tube. We employed the LP to evaluate the plasma potential downstream at the location of the RPA as a correction to the most probable voltage on centerline. This correction is necessary since the bias voltage on the ion selection grid of the RPA is relative to facility ground, not the local plasma potential.
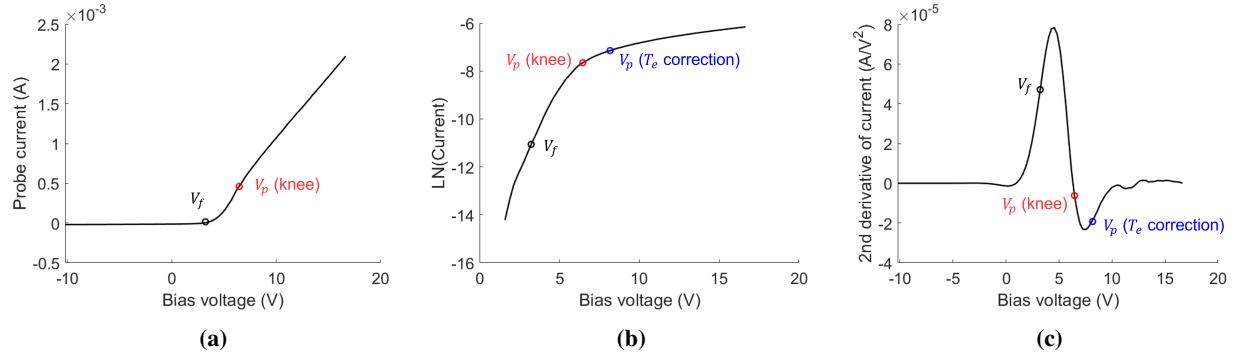

(a) (b) (c)

Fig. 7 Langmuir probe data for xenon at 300 V, 125 A. (a) Raw probe I-V trace. (b) Electron temperature fit to the log of electron current. (c) Second derivative zero crossing method for determining the plasma potential. In all cases, the electron retarding region is between the black and the red circles.

Figure 7 represents an example of raw and processed data for xenon operation at 300 V and 125 A. We typically swept the potential of the LP from a bias voltage of $V_b = -10$ V to $V_b = +30$ V and measured the resultant current from the plasma via a picoammeter. As depicted in Fig. 7b, we inferred the electron temperature by subtracting the ion current (the region from approximately -10 V to 0 V) from the raw trace, then fitting a line in log space to the resulting electron current signal, I_e, as a function of V_b in the electron retarding region. The inverse slope of this line yielded T_e. We neglected uncertainty in our reporting of this value. This methodology follows best practices as outlined in Ref. [40].

We estimate the plasma potential from the Langmuir probe trace in two ways. First, we used classical Maxwellian theory for probe analysis to relate the floating potential V_f to the plasma potential, V_p(Te correction) = V_f + $T_e \ln\left(\sqrt{m_i/(2\pi m_e)}\right)$. The result of this analysis is shown as a blue marker in Fig. 7. As an alternative method for evaluating the plasma potential, we used the zero crossing in the second derivative (Fig. 7c) of electron current, i.e. the "knee" potential, V_p(knee). The potential determined from this method is shown as a red marker in Fig. 7. Due to noise in the raw Langmuir probe data at low currents, we were unable to obtain a clean estimate of V_p with the "knee" method

11

at every condition. We therefore used the Maxwellian method to determine V_p at all conditions, and treat the difference between the two methods for calculating V_p at conditions where $V_p(\text{knee})$ was able to be determined as a characteristic uncertainty.

E. E×B probe

The E×B probe serves as a mass spectrometer, determining the quantity of different charge species within the thruster plume. These fractional charge species inform the calculation of the charge utilization efficiency (Eq. 7). Existing within the E×B probe are orthogonal radial and electric fields. When an ion passes through the probe with some axial velocity, the force from the electric field and from the magnetic force acting on the velocity of the ion must be balanced in order for the ion to intercept the collector at the back of the probe. Because ions have a velocity proportional to their square root of charge, the probe can isolate different charge state populations in this manner.

The E×B probe we employed for this study had an entrance aperture 1.6 mm in diameter, an entrance collimator 7.5 cm long, an exit collimator 15 cm long, and electrical plates spaced 0.97 cm apart. The peak magnetic field was 0.16 T in the center of the probe. We swept the applied bias voltage to the plates from 0 to 80 V at lower current densities and up to 100 V at higher current densities to capture all the multiply-charged species content.
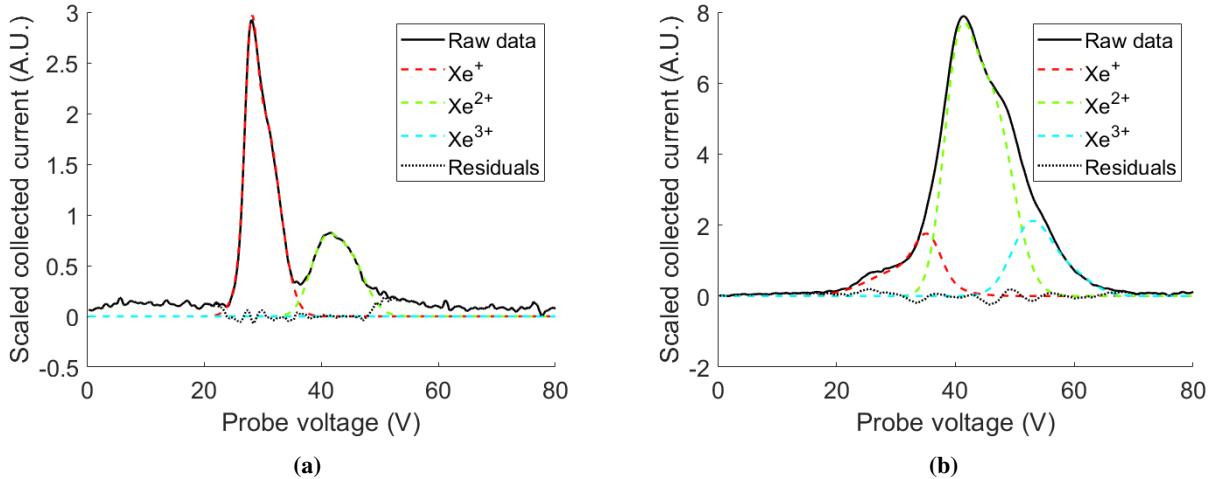

(a) **(b)**

Fig. 8   Raw E×B trace and two-peak Gaussian fits for all charge species of xenon at a) 300 V and 15 A and b) 300 V and 125 A.

We show in Fig. 8 examples of raw traces from the probe at two operating conditions. The peaks in these results correspond qualitatively to the relative currents in each charged species. To determine the charge fraction, Ω_i, of each of these species, we follow the approach in Ref. [41] where we fit dual Gaussian distributions to each peak in the raw trace. This previous work showed that a dual Gaussian functional form best captures the high-velocity tail often seen in Hall thruster ion velocity distributions, a finding also reflected in our own work [30]. In our procedure, we fitted the two-peak Gaussian to the location we anticipated the singly-charged species to be at for a given propellant based on the 15 A trace where singly-charged ions dominate. We subtracted this fit from the raw trace and repeated this process up to three charge states. By integrating the area of the fit for each peak and comparing it to the total integrated area under the trace, we obtained uncorrected charge fractions.

Due to the presence of finite background pressure in the facility, we needed to modify the raw charge fractions to account for the presence of charge exchange (CEX) ions. To this end, we followed the methodology outlined in Refs. [30, 42, 43] where the corrected charge fraction is given as

$$\Omega_i = \frac{\Omega_{i,raw}\left(j/j_0\right)_i^{-1}}{\sum_k \left(\Omega_{k,raw}\left(j/j_0\right)_k^{-1}\right)}. \tag{12}$$

Here the $\left(j/j_0\right)^{-1}$ term is the CEX correctional factor and the summation over k is the total area under the fitted curves. These correctional factors for the charge fractions are dependent on ionization cross-sections and background neutral

12

density in the chamber and are taken from Refs. [44, 45] following the process outlined in our previous work [30]. These values are shown in Appendix A. As mentioned in Sec. II.B, we saw atypically low background pressures during testing—approximately ∼1.8× previously recorded values at the same conditions [20, 30]. To accommodate this uncertainty, we applied a correction factor of 1.4× to our recorded pressures when evaluating Eq. 16, accompanied by a 40% error to include both the original value and the 'corrected' value that is 1.8× higher. The error associated with this correction was propagated through to the charge utilization efficiency, Eq. 7, following the methodology in Ref. [43].

F. Faraday probe

Faraday probes can be used to determine beam plasma characteristics by biasing them to a sufficiently negative voltage such that they only collect ion saturation current. These measurements of the beam current in turn inform estimates for the beam utilization efficiency (Eq. 6), mass utilization efficiency (Eq. 8), and divergence efficiency (Eq. 10). In practice, a guard ring around the central probe collector disc is used to maintain a constant effective probe area. By measuring the collected current of the central probe during an azimuthal sweep of the probe through the plume at constant radial distance from the thruster, we can plot a distribution of the current density. From this, we can determine both the beam current and divergence angle.

The Faraday probe employed in our experiment was mounted on a rotational probe arm located ∼$10.5D_T$ downstream of the thruster exit plane (Fig. 5a). The Faraday probe used had a 1.74 cm inner diameter molybdenum collector and 2.38 cm outer diameter molybdenum guard ring, with a 0.05 gap between them. It was biased to -30 V during probe sweeps. During operation, the Faraday probe was swept from 0 to 180 degrees and back again with respect to thruster centerline, and the resultant trace was separated into four sections from centerline to the edge (i.e. 0 to 90, 90 to 180, 180 to 90, and 90 to 0 degrees).

The current collected by the probe as a function of angle was converted to current density per the relation identified in Ref. [46]:

$$j = \frac{I_{FP}}{A_C + \kappa_G} \kappa_{SEE},,$$ (13)

where I_{FP} is the current collected by the Faraday probe, A_C is the collector area, and κ_G and κ_{SEE} are corrections factors arising from geometric and secondary electron emission (SEE) effects respectively [46]. These corrections are described for our probe geometry and for both krypton and xenon in Appendix A.
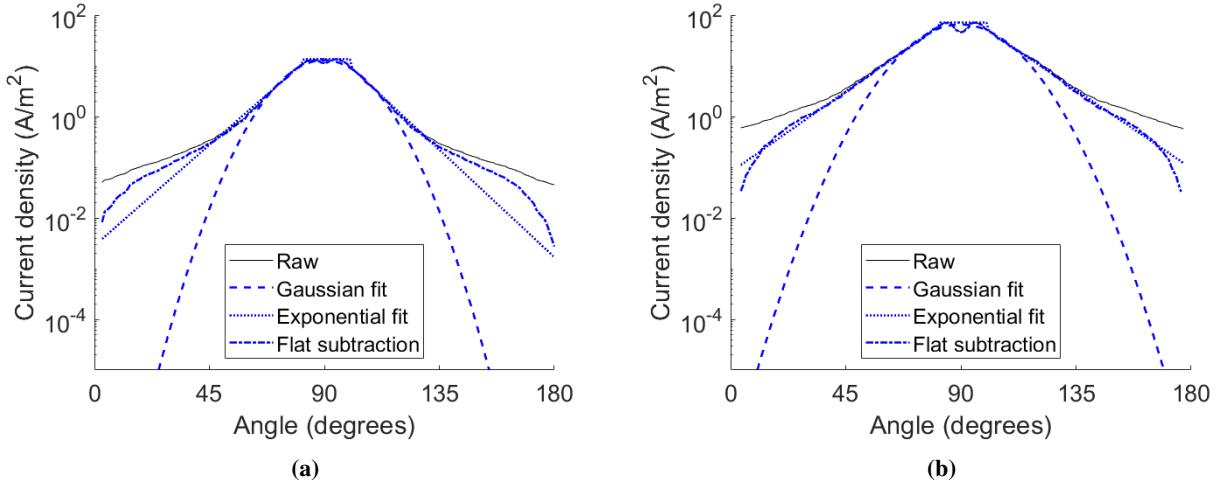

(a)   (b)

Fig. 9 Raw current density trace from Faraday probe and different CEX correctional methods during operation on xenon at) 300 V and 15 A and b) 300 V and 125 A.

As with the E×B probe, the current density trace needed to be corrected for effects related to the background pressure in the facility. The dominant factor is the effect of ions from charge exchange (CEX)—fast neutrals and slow ions resulting from collisions between slow neutrals and fast ions in the beam. We used three different methods to

correct for this CEX effect: a Gaussian fit [46], an exponential fit [41], and a flat subtraction [47]. These different fits are shown for two different conditions in Fig. 9.

The beam current was calculated for each segment and fitting method as

$$I_b = 2\pi R^2 \int_0^{\pi/2} j(\theta) \cos\theta \, d\theta, \tag{14}$$

where R is the distance from the exit plane of the thruster to the probe and θ is the azimuthal location of the probe in radians. For each of the four sweep segments, an average beam current was determined using an ensemble modeling method by averaging I_b as calculated by the Gaussian, exponential, and flat subtraction methods. The uncertainty for the beam current was then calculated as twice the standard deviation in the average value between the four segments. We used the resulting values of beam current in the estimates for beam utilization and mass utilization efficiencies.

We determined the divergence angle as [46]

$$\cos\theta_d = \frac{\int_0^{\pi/2} j(\theta) \cos\theta \sin\theta \, d\theta}{\int_0^{\pi/2} j(\theta) \cos\theta \, d\theta}. \tag{15}$$

For this parameter, we used only the corrected current density trace from the exponential fit method. This is because the Gaussian fit and flat subtraction methods have not been shown to yield accurate estimations of divergence angle without extrapolating back to the exit plane of the thruster [30, 46, 47]. As we did not take Faraday probe traces at multiple radial distances, fitting the downstream divergence back to the thruster exit plane was not possible. The exponential fit method has been used previously to calculate divergence angle without any additional extrapolation [41], so this method alone was selected for divergence angle calculations. Once we found the beam divergence, we in turn employed it to estimate the divergence efficiency (Eq. 10).

G. QCM

Given the high rates of mass flux from the thruster in this campaign, it is important to quantify the degree of backsputter in the facility. To this end, we employed a Quartz Crystal Microbalance (QCM) sensor to measure the rate of carbon backsputter in the plane of the thruster from the graphite beam dump and probe shield. The QCM estimates the total mass deposition by determining the change in the resonant frequency of a quartz crystal as material is deposited. Total deposition, or thickness t, was calculated with the relation $t = (K\Delta f)/d$, where Δf is the change in frequency, K is a constant, and d is the density of the material deposited [48]. We assume in this work that only graphite was deposited onto the thruster for these measurements.

For this effort, we employed a INFICON QCM front load single sensor mounted 1 m from the thruster and aligned with the plane of the thruster facing downstream (Fig. 2). Attached to the sensor were cooling lines connected in parallel to the thrust stand cooling system to regulate the temperature. The rate of deposition was calculated with the device by determining the slope of the thickness measurements over time.

H. Thruster and facility health monitors

Given that the primary goal of this effort was to explore the operation of a Hall thruster at atypically high current densities, we implemented a series of diagnostics to monitor thruster heath in real time. To this end, we employed eleven thermocouples installed at various locations in and around the thruster body. The most critical thermocouple was located on the inner front pole (IFP), which reached the highest temperatures of all the monitored regions on the thruster. Additional thermocouples were placed at various locations on the thrust stand, the cooling system, and the crypopumps. One thermocouple also monitored the temperature on the APC motion stage to ensure that it did not overheat at the high current conditions.

Oscillations in discharge current, cathode current, discharge voltage, and cathode-to-ground voltage were monitored with a Keysight DSOX 3024A oscilloscope. The primary metric of interest for this campaign was the relative peak to peak oscillation in the discharge current. We did not, however, record time series to estimate the spectral content. For visual inspection of the thruster, we mounted an Ethernet camera (Sanyo model VCC-HD2500P) on the azimuthal probe arm adjacent to the Faraday probe (Fig. 2). The camera was placed behind a sacrificial glass optic and had no difficulty operating in vacuum or for brief periods in the thruster plume as the arm was swept. Thruster and facility health telemetry including real time temperatures, oscillation strengths, and DC supply currents and voltages were monitored via an optically-isolated, automatically-logged data acquisition system.

14

V. Results

We present in this section the results of our experimental characterization of the thruster operating on both xenon and krypton at 300 V and discharge currents ranging from 15 to 150 A. We first report on the global performance metrics including thrust, specific impulse, and efficiency. We then present the processed results of individual probe measurements. We in turn convert these measurements into estimates for the thruster efficiency modes. We conclude with an overview of key parameters related to thruster and facility health including oscillation levels, temperature data, carbon deposition rates, and facility pressures.
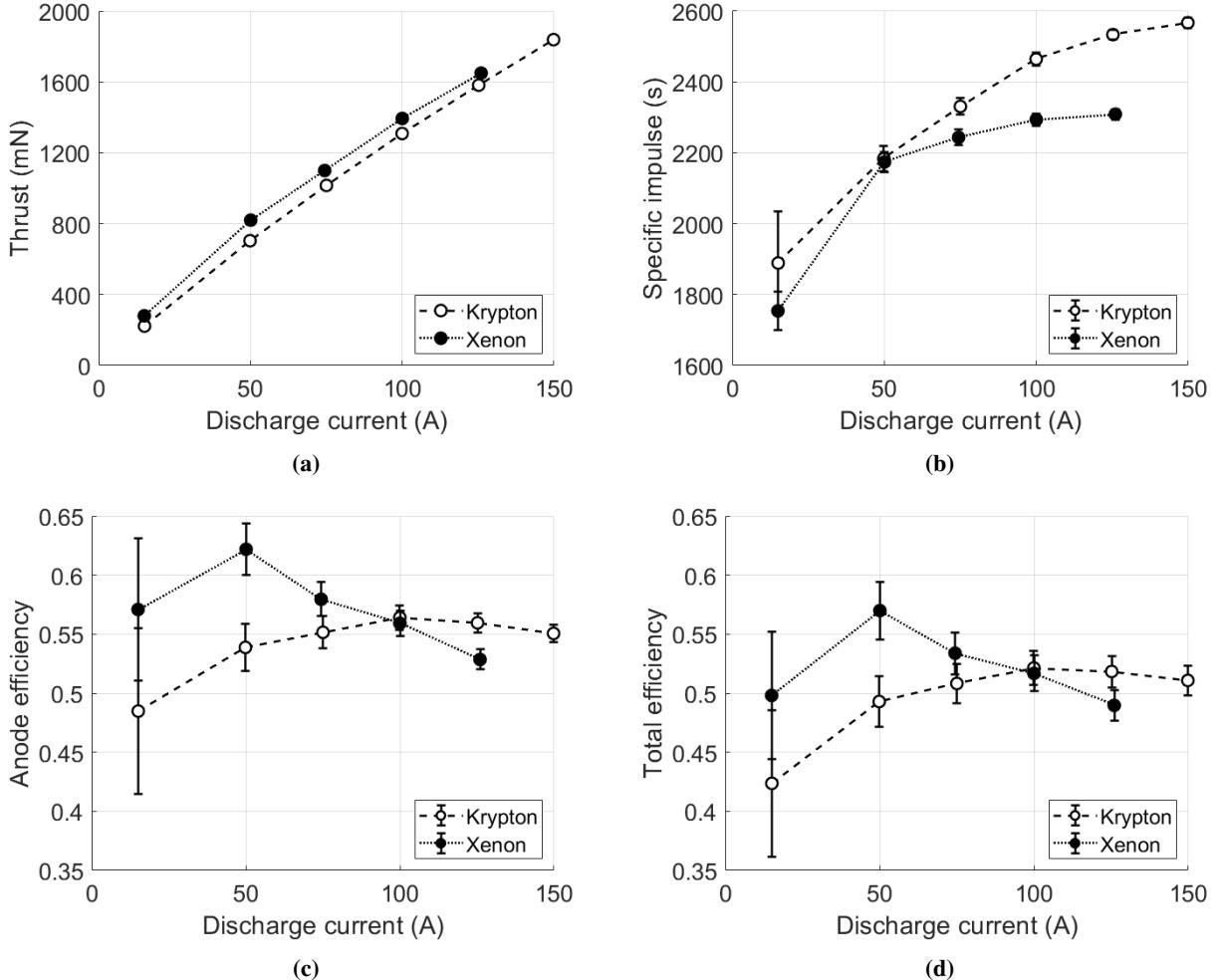
A. Global performance

Fig. 10   a) Thrust, b) specific impulse, c) anode efficiency, and b) total efficiency at 300 V for both xenon and krypton with varying discharge current. Note that the uncertainties in Fig. 10a are smaller than the marker sizes.

Figure 10 presents the thrust, specific impulse, anode efficiencies, and total efficiencies for both propellants at all conditions. Exact values are tabulated in the Appendix in Tables 5 and 6. As can be seen from Fig. 10a, the thrust trends approximately linearly across the range of currents for each propellant. The xenon thrust exceeded krypton at all discharge currents; at the maximum current where we tested both gases, 125 A, xenon reached 1650 ±10 mN and krypton 1582 ±8 mN. Krypton achieved the maximum overall thrust recorded from this effort with a value of 1839 ±10 mN at the 150 A condition. We note here that the thrust for both propellants measured at the 4.5 kW condition were ~14 mN (or 4–6%) lower than those previously measured on the H9 [30]. We attribute this discrepancy to differences between the baseline H9 and modified test article we used in this campaign, such as changes in material and electrical

configuration (e.g. body tied to ground instead of body tied to cathode). Most saliently, this may have been caused by the switch from a BN to graphite chamber, which has been shown to slightly decrease performance on other shielded thrusters [27, 31].

As shown in Fig. 10b, the specific impulses measured during krypton performance were all higher than that of xenon at the same discharge current. At 150 A, krypton operation showed a specific impulse of 2567 ±16 s. At 125 A, krypton yielded a specific impulse of 2534 ±15 s and xenon resulted in 2309 ±17 s. This disparity can be attributed to the fact that krypton is a lighter atom. As discharge voltage remained the same at each test point, the similar amount of electrostatic acceleration resulted in higher exit velocities and specific impulse for krypton, the lighter gas. This follows from the relation for singly charged ions that $I_{sp,th} = \sqrt{2qV_d/m_i}/g_0$. Similar comparisons between krypton and xenon specific impulse have been reported in previous studies [30, 49–56]. The disparity in specific impulse also can explain the differences in thrust exhibited by Fig. 10a. As thrust-to-power scales inversely with specific impulse, xenon—which has a heavier mass per atom—has a lower specific impulse and higher thrust at fixed power.

We note here that for a beam of only singly-charged ions at 300 V, the theoretical limit is 2140 s for xenon and 2680 s for krypton. However, as seen in Fig.10b, xenon surpasses this theoretical limit at the 50 A condition, while krypton approaches its limit at 150 A. We attribute this to the high population of multiply-charged species in the beam, particularly for xenon at higher currents (see Sec. V.B). We discuss this trend further detail in Sec. VI.A.

Figure 10c shows the anode efficiency for both propellants. For each gas, the efficiency trend exhibits non-monotonic behavior, peaking at given power before decreasing. The maximum for xenon occurred at 50 A with an efficiency of 62.2 ±2.2%, while the maximum for krypton occurred at 100 A with 56.4 ±1.0%. Practically, we remark that although it is evident that the efficiency does decrease with higher current, the efficiency across the current range is still competitive with state of the art Hall thrusters that operate at lower currents. The lack of a marked decrease in efficiency with current (and current density) is an indication that the scaling laws that previously have governed Hall thruster sizing may not be absolute. This has direct implications for achievable thrust density of Hall thrusters at higher power (see Sec. VI.E).

In terms of the non-monotonic trend in efficiency, we ultimately conjecture that this is the result of a trade between improved mass utilization and reduced beam utilization efficiencies. Thus, we theorize that krypton's efficiency peaks at a higher current due to its relatively lower mass utilization at low-current density conditions. We discuss this in further detail in Sec. VI.B. Also of note is that at the 100 and 125 A conditions, the efficiency of krypton becomes higher than that of xenon. Although we were not able to take data at the 150 A condition for xenon, we postulate that the downwards trend continues and the gap between xenon and krypton may widen.

The trends in total efficiency, shown in Fig. 10d, closely mirror the trends in anode efficiency. The magnitudes are ~4–7% lower, however, because we now account for the flow through the cathode and the power supplied to the magnets. Xenon's total efficiency ranges from 49.0–57.0%, while krypton's ranges from 42.4–52.1%. There is a slightly steeper increase between the efficiency at the 15 A and the 50 A condition for both propellants due to the relative fraction of total power going towards the magnets at lower discharge powers. The crossover point between xenon and krypton takes place at the same condition of 100 A, and the overall trends for both propellants are the same as for anode efficiency.

B. Probe measurements

We present in this section the processed results of our far-field probe measurements as a function of operating condition. We first show in Fig.11 the plasma potential and electron temperature as calculated from Langmuir probe traces using the methodology outlined in Sec. IV.D. The electron temperature and the plasma potential generally trend downwards after achieving a maximum value with increasing discharge current. This trend suggests that for the most part, the electrical coupling between cathode and the main discharge is improving with higher discharge currents [57]. This trend in xenon plasma potential decreasing with increasing current is in line with behavior seen on this thruster in previous work [20].

We show in Fig. 12 the average ion energy inferred from the RPA for both xenon and krypton. In this case, we have made a correction to the RPA measurement with respect to ground by subtracting the local plasma potential as determined by the LP. The ion energy per unit charge within error bars is on the order of the applied voltage of 300 V. This is consistent with the electrostatic acceleration imparted on the ions. Notably, the average ion energy increases monotonically with xenon while trending down with krypton. This may suggest that the acceleration process for each propellant is impacted in opposing ways on by the increasing current density in the thruster.

In Fig. 13 we present the charge fractions as calculated from the E×B data at all conditions. For both propellants, we see that the fraction of the singly charged state generally decreases while the population of the multiply charged state increases. Indeed, xenon exhibits a population inversion (i.e. where the fraction of doubly charged ions surpasses
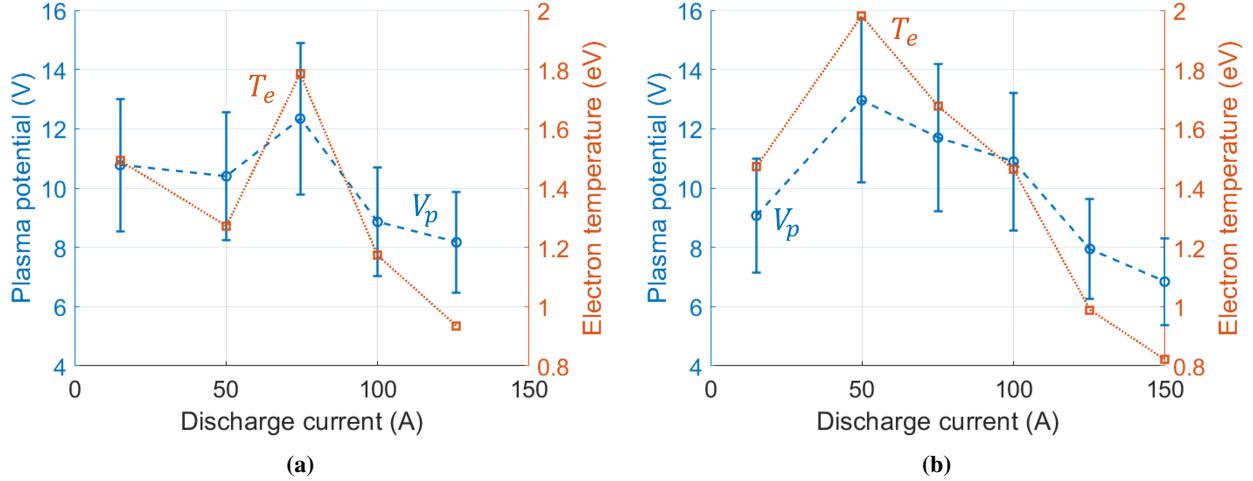
Fig. 11   Plasma potential and electron temperature of a) xenon and b) krypton at 300 V with increasing discharge current.
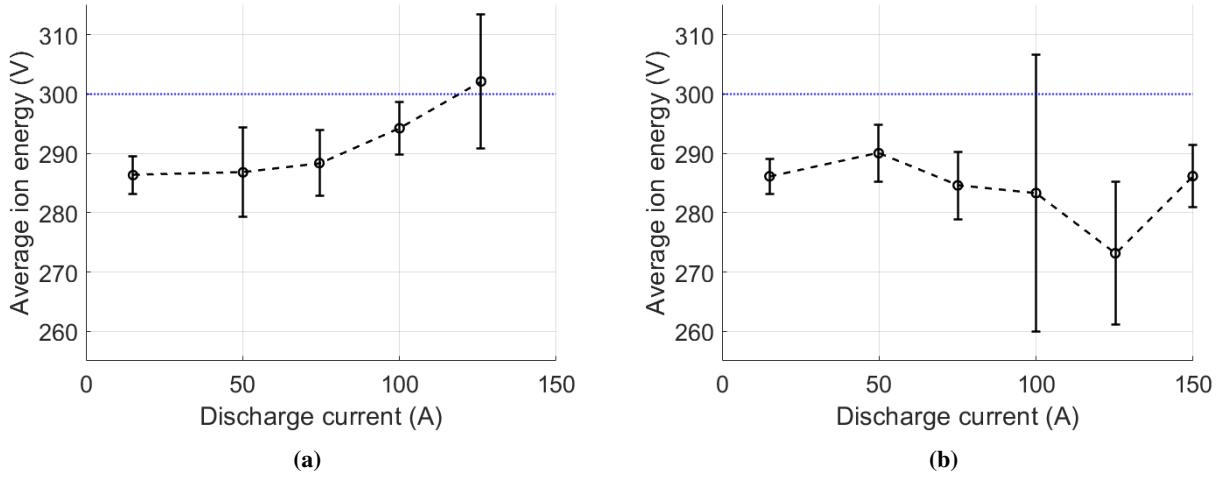

Fig. 12   Average ion energy inferred from RPA corrected by the plasma potential for a) xenon and b) krypton at 300 V with varying discharge current. The discharge voltage is indicated with a dotted blue line.

that of singly) between 50 and 75 A. While krypton never reaches this point, we see in Fig. 13b that it approaches a population inversion with both singly and doubly charged species making up approximately half of the beam at the highest current condition of 150 A. These trends may in part be explained by the correlation between increased plasma density and current density in the channel with higher discharge current. As current densities increase, mass utilization efficiencies approach unity (see Sec. V.C). This is because more of the inlet propellant is ionized due to the higher plasma density. In turn, there are more collisions between the resulting singly-charged ions and electrons which may explain the higher densities of multiply-charged species. Relatedly, we note that the triply-charged population also appears to be steadily increasing for xenon, although for krypton it stays fairly constant. This may be attributed to the higher required ionization energies for triply-charged krypton compared to xenon.

In Fig. 14, we show the beam current as determined from the three different methods outlined in Sec. IV.F at all conditions for both xenon and krypton. The spread in beam currents for a given method and discharge current stems from the four spatially distinct segments of the Faraday probe trace we used in our analysis. With the exception of the 50 A xenon condition (which had a variation of up to 6%), all methods exhibited less than 3% variation among the four segments. The actual magnitudes of the beam current within each method differed, however. As can be seen,
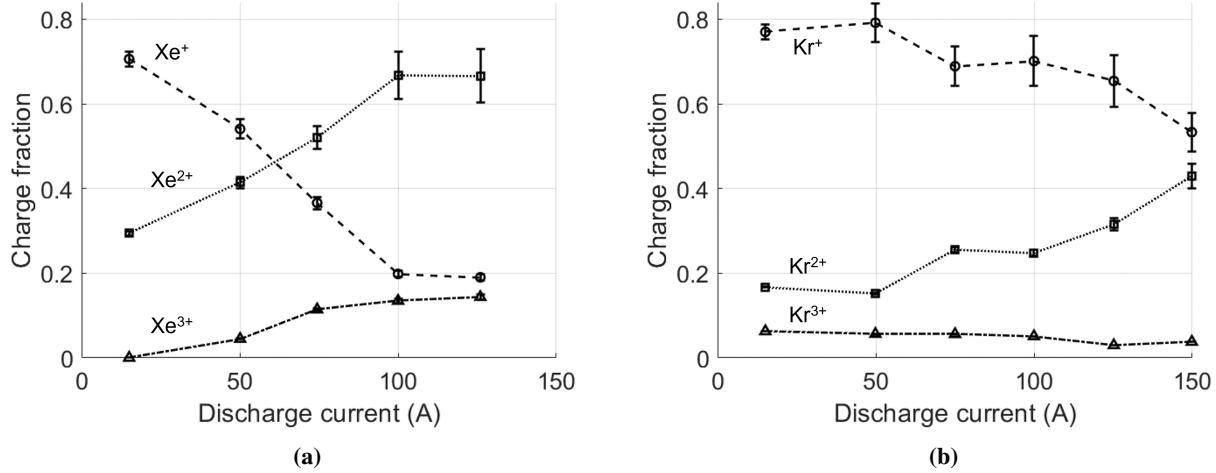
17

Fig. 13 Charge fractions of singly, doubly, and triply ionized a) xenon and b) krypton at 300 V with varying discharge current.

the exponential and flat subtraction methods both resulted in higher values of the estimated beam current while the Gaussian method underestimated the beam current. We ultimately used the average of each model for our mean value of beam current. The variation in predicted current in turn stemmed from the variation across the four beam segments. Physically, we see that the beam current for all methods was approximately linear with total discharge current. This reflects the fact that the total ion current downstream of the thruster is directly linked to the total current sourced by the thruster.
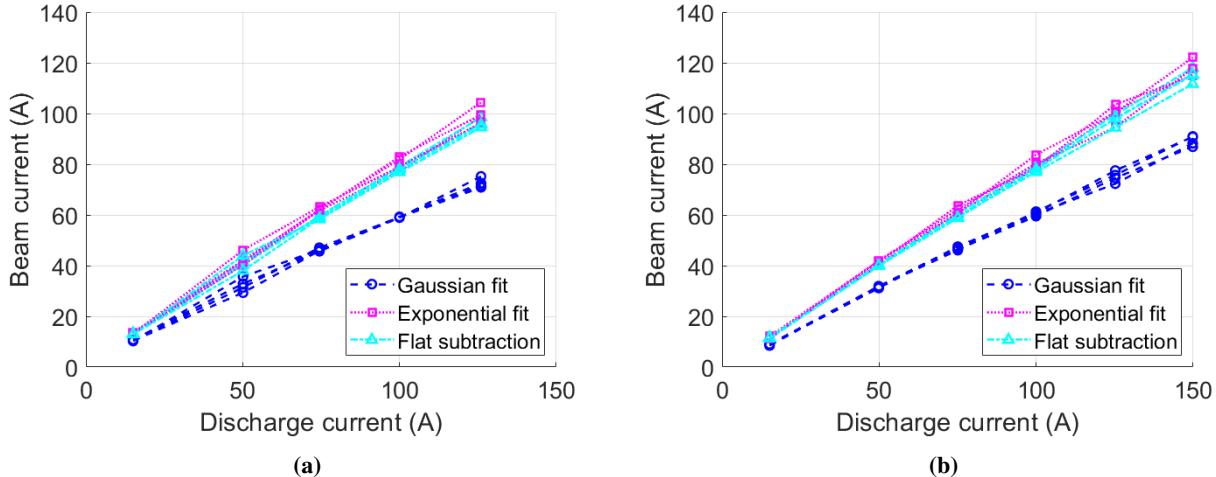

Fig. 14 Beam current as calculated using different CEX correction methods for a) xenon and b) krypton at 300 V with varying discharge current.

Figure 15 shows the plume divergence angles as calculated by the exponential fit method (see Sec. IV.F). For xenon, this angle monotonically increased with current from $22.5° \pm 0.7°$ at 15 A to $28.2° \pm 0.7°$ at 125 A. The range of values is consistent with previously reported values on the H9 [30, 58]. Physically, our result indicates that the beam became increasingly divergent with increased current in the xenon case. In contrast, for krypton, there is less of a clear trend as discharge current increases. Indeed, the divergence angle stays almost the same for all currents, only ranging from $26.5° \pm 0.5°$ at 50 A to $27.9° \pm 0.7°$ at 150 A.
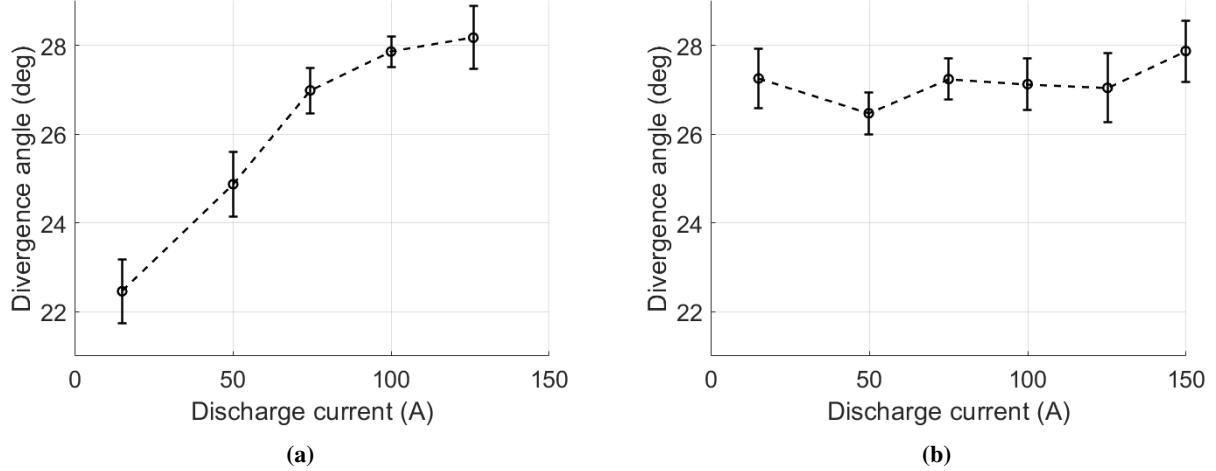
18

Fig. 15   Plume divergence angle of a) xenon and b) krypton at 300 V with varying discharge current.

C. Efficiency analysis

We show in Fig. 16 the trends in calculated efficiency modes as a function of discharge current for both propellants. These estimates are based on the far-field plasma measurements reported from the previous section. The uncertainty in these values stems from the propagation of experimental error through the governing equations of the efficiencies (sec. III.B). Additionally, we compare the anode efficiency as calculated by the product of partial efficiencies (Eq. 5) to the anode efficiency as calculated from thrust measurements. We discuss in the following section key trends in each component of the efficiency.

1. Anode efficiency

The black line in Fig. 16 indicates the anode efficiency as calculated as the product of partial efficiencies (Eq. 5), while the gray line indicates the anode efficiency as calculated from thrust data (Eq. 3). For both propellants at all conditions, $\eta_{a,probe}$ and $\eta_{a,thrust}$ are within uncertainty of each other. This indicates that the efficiency model outlined in Fig. III.B is an accurate representation for the performance of the thruster. Both methods of calculating anode efficiency also follow the same general trends. For xenon, both anode efficiencies peak at 50 A, and for krypton, both anode efficiencies peak at 100 A. The increasing trend in efficiency with current at lower currents for krypton operation is in line with previous observations [52].

2. Beam current utilization

The beam current utilization steadily decreases for xenon with increasing current. With krypton, the current utilization efficiency increases from 15 to 50 A before decreasing throughout the higher current conditions. This downwards trend in beam utilization efficiency is broadly consistent with previous studies of Hall thruster efficiency at high powers, and the values are in line with what is typically observed on Hall thrusters[16, 20, 59–65]. This behavior suggests that electron confinement decreases at higher currents, leading to a higher relative contribution of electron current to the total current. This behavior is broadly consistent with past phenomenological explanations that have been proposed (c.f. [14, 16]) for the impact of plasma density within the discharge channel on Hall thruster operation. Indeed, it has been suggested in these works that the higher plasma density associated with higher current density will lead to enhanced electron collisionality and therefore higher degrees of cross-field electron transport. Notably, however, we see that the degree of change in the beam utilization efficiency is only ~5% over an order of magnitude increase in current. This suggests that the loss of electron confinement is not driving the overall performance to non-competitive values. Indeed, the relatively gradual downwards trend in beam utilization largely explains why the thruster performance has not suffered markedly at these high-current conditions. This behavior is further explored in Sec. VI.B.

19

3. Charge utilization

As can be seen from Fig. 16, the charge utilization is nearly unity for the range of investigated currents. The uncertainties on these reported values are comparatively large (>±5%), especially at the higher current conditions. This is due to the uncertainty associated with the correction applied to the background pressures. In actuality, the charge utilization has a floor at about 94% in a situation where there are an equal amount of singly, doubly, and triply-charged ions, and a ceiling at 100% in a situation where there is only one species in the beam. The error bars shown in Fig. 16 are therefore an overestimate of the actual uncertainty.

With respect to physical trends in the data, we see that for xenon, there is a minor decrease in charge utilization in the range from 50–75 A before increasing again. This behavior can be explained by the relative disparity of charge states—charge utilization is ultimately 100% when the beam is mono-energetic and deviates from this when the beam is polydispersive. At low currents for the xenon case, the beam is composed of mostly singly-charged particles (Fig. 13). The charge utilization reaches a minimum for xenon at 75 A, which is where the populations of singly and doubly-charged particles invert. After this inversion, the doubly-charged particles become dominant and the beam once again approaches monoenergetic. For krypton, on the other hand, the charge population never inverts. As a result, the charge utilization decreases throughout the entire range of currents.
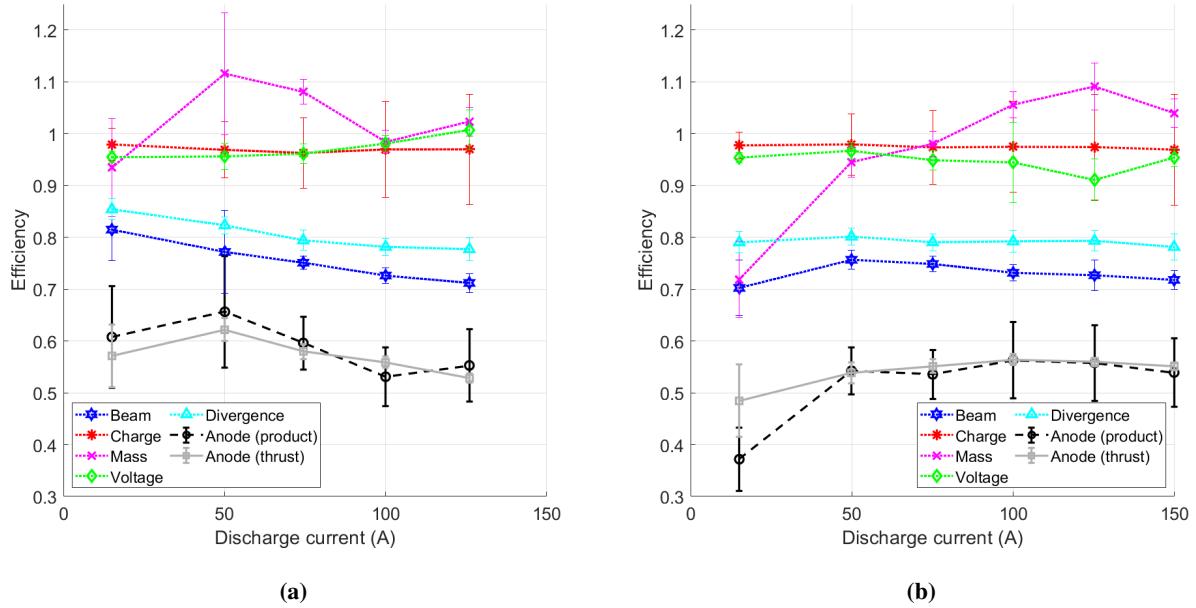

(a)

(b)

Fig. 16   Efficiency modes for a) xenon and b) krypton at 300 V with varying discharge current.

4. Mass utilization

The mass utilization for both xenon and krypton is below 100% at the 15 A discharge current conditions. For krypton in particular, the mass utilization at these currents is one of the two lowest partial efficiencies (at ~72%). This in line with previous results indicating low mass utilization for krypton at typical Hall thruster current densities [30, 51–54, 56].

With increasing current for both gases, the mass utilization exceeds 100%. The underlying reason for this is not clear, though it may in part be attributed to the limitations of our attempts to deconvolve the impact of CEX ions or to the validity of key assumptions underlying our calculation. To the former point, an excess of CEX particles in the probe trace, which result from the high background pressures, may artificially inflate our estimates for the total beam current. Our methods to eliminate this effect may be insufficient (Sec. IV.F). To the latter point, it is common to assume that cathode ions have a negligible contribution to the downstream current density. This stems from the fact that the majority of current from the cathode is carried by electrons. With that said, if any of the neutrals from the cathode are in fact ionized and accelerated through a sufficient potential drop to significantly contribute to current density, this could manifest as a higher-than-unity efficiency in the mass utilization. This process may be a possibility given the atypical

operating conditions for the thruster, and indeed, it would explain why we only see the mass utilization exceed 100% when the discharge current exceeds the nominal maximum 20 A of the H9.

With that said, in our subsequent discussion, we work under the assumption that in practice, the total mass utilization efficiency is effectively 100% whenever the measured value exceeds this value. This is physically consistent with the interpretation that the plasma density at these conditions is sufficiently high that all inlet neutral gas is ionized.

5. Voltage utilization

The voltage utilization is calculated by using the RPA ion energies corrected for plasma potential as measured by the LP. As can be seen from Fig. 16, for xenon, the voltage utilization monotonically increases as current increases. This is consistent with the trends exhibited in Fig. 12 where we see the average ion energy increases with discharge current. For krypton, all points are within uncertainty of each other (a minimum of 91.1 ±4.0% and a maximum of 96.7 ±1.7%), indicating no clear change in this efficiency mode with increasing current.

6. Plume divergence

As seen in Fig. 15a, the plume of the thruster operating on xenon continuously expands as the current increases. This trend is reflected in Fig. 16a, where we see the plume divergence efficiency monotonically decreasing for xenon. The behavior of krypton's divergence angle, which stays fairly constant throughout the range of currents, is also reflected in the nearly-constant divergence efficiency of krypton as seen in Fig. 16b. The plume divergence represents the second-largest detractor to the overall efficiency (next to beam utilization) for both propellants at all conditions.

D. Oscillation level

In order to characterize the stability of the thruster, we show in Fig. 17 the magnitude of the peak-to-peak oscillations in the discharge current relative to the mean value. The uncertainty on these oscillations was determined by taking the twice the standard deviation in the peak-to-peak oscillation strength over ten seconds. For xenon, we see that the current oscillations monotonically decreased with discharge current, starting at 69% at 15 A and ending at 4% at 125 A. We remark here that this latter value is exceptionally low for Hall thrusters [66]. For krypton, the current oscillations generally decreased but exhibited a minor inflection from 75 and 100 A. The oscillation levels for this gas ranged from an oscillation strength of 43% at 15 A to 19% at 150 A. From a practical perspective, these measured levels of oscillation show that the thruster did not exhibit unusually high oscillation modes with increasing current density. This suggests that at least for this configuration, a high current density Hall thruster has not only comparatively high performance but is also stable.
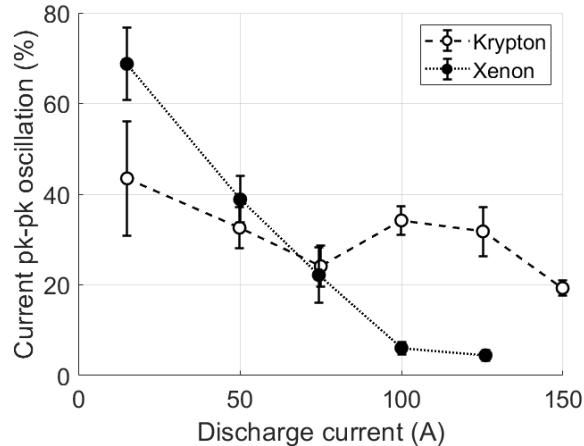

Fig. 17   Ratio of peak-to-peak oscillation to mean value of discharge current at 300 V for both xenon and krypton with varying discharge current.

E. Thermal

In Fig. 18, we show the temperature of the inner front pole (IFP) and corresponding discharge current throughout a testing day. The times at which the current goes to zero instantaneously are thrust points or unexpected shutdowns. The rate of temperature increase steepens at higher currents as is expected due to the increased power deposition to the walls and other surfaces of the thruster. During xenon operation, we were able to maintain IFP temperatures below an internally-defined red limit. This limit is based on concerns for the health of the thruster magnetic circuit. For krypton at 150 A, the IFP temperature did briefly cross this limit, but this was deemed an acceptable risk to collect all necessary data at this condition. The typical ramp time to achieve each power level was 5–10 minutes. The total time spent at each power condition varied from 5–15 minutes with a total of 10 minutes at the maximum power of 150 A and 300 V (45 kW) on krypton.

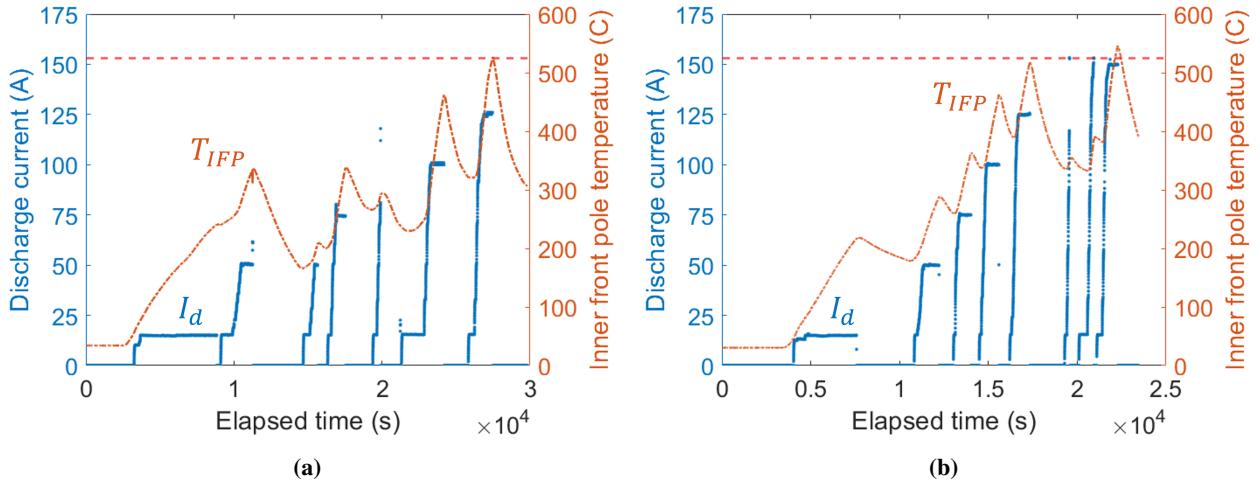(a)   (b)

Fig. 18   Discharge current and inner front pole temperature throughout a testing day for a) xenon and b) krypton at 300 V. The dashed red line indicates the temperature limit for the IFP.

F. Facility

We present in this section two metrics for evaluating the response of the facility to the thruster at high current density operation. First, we show in Fig. 19a the carbon deposition rate as a function of discharge current. For comparison, we show as a horizontal line on this plot a value of 30 μm/kh. This is a typical erosion rate reported for the pole covers of the HERMeS 12.5 kW class magnetically shielded Hall thruster [23]. The key insight from this result is that the deposition rate increases with total current from the thruster. This physically stems from the fact that the sputter rate is proportional to total incident flux on the facility surfaces. Xenon shows a marginally higher rate at each power level, which could be a result of the difference in the mass of the ions. Practically, we see that above 75 A, typical thruster erosion rates are surpassed. This highlights a potential problem with thruster testing at these unprecedented high power levels where the rate of deposition of the facility may mask erosion on the surfaces. We qualify this observation with the fact that it is also possible that erosion rates will scale with current density as well such that the relative ratio may remain unchanged. This type of trend should be the subject of future study [24].

As a second notable trend, we show in Fig. 19b the facility pressure as a function of discharge current. In this case, we have included uncertainty bars to reflect our relative lack of confidence in the most recent pressure gauge calibration. We also show for comparison on this plot the Randolph standard of 10 μTorr-Xe, which previously has been proposed as a maximum allowable pressure for performance testing of lower power Hall thrusters [67]. It is immediately evident from this result that even at 75 A (22.5 kW) of testing power, the pressures in the facility exceed this limit. This again underscores the challenges with how to translate ground test results of high power systems to be representative of flight [24].
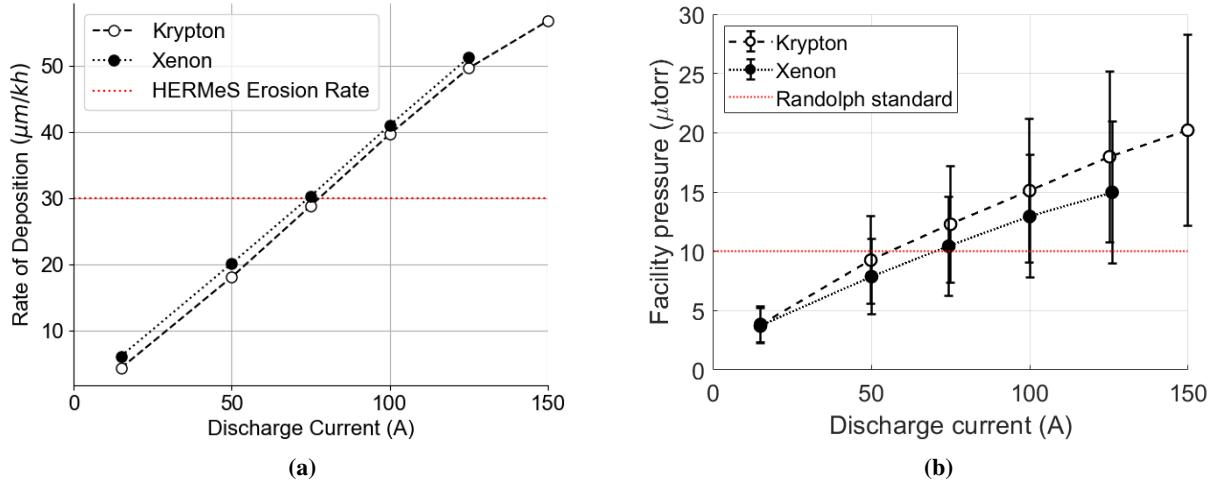
Fig. 19 a) Carbon deposition rate and b) facility pressure for at 300 V for both xenon and krypton with varying discharge current. The relatively large uncertainties on pressure are due to the discrepancy between pressures measured during this campaign and pressure reported in previous campaigns.

VI. Discussion

In this section, we discuss key implications of our results. We first remark on explanations for notable trends in the specific impulse, efficiency, and oscillation level. We then remark on the challenges of facility effects highlighted by this study. We conclude with a discussion of the impact of our results on our fundamental understanding of the limits of Hall thrusters for operation at high power and their comparative advantages to other technologies.
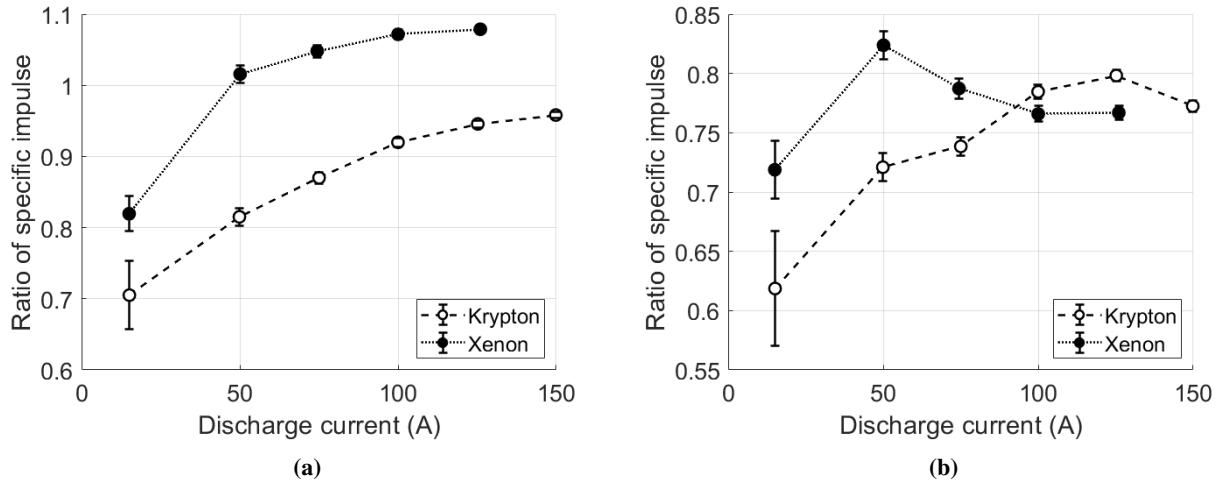
A. Trends in specific impulse

Fig. 20 Ratio of actual specific impulse to theoretical limit for both xenon and krypton at 300 V as calculated with a beam that a) is fully singly-charged b) has an effective charge state as determined by the E×B probe.

As shown in Sec. V.B, one of the notable results of our study is that the charge fraction for doubly and triply charged species increases significantly with discharge current. As we discussed in the preceding section, one explanation for this behavior may be attributed to the fact that at high discharge currents, the number density of electrons in the channel is sufficiently high to completely ionize the gas before it transits the channel (i.e. the mass utilization efficiency approaches

unity). In turn, at these high currents, the resulting singly-charged ions can have additional ionization events to gain additional charge. This explanation is reflected in the trends shown in Fig. 13 for both xenon and krypton. For xenon at currents above 75 A, doubles become the dominant species. For krypton, it appears that this transition may occur at currents above 150 A.

One of the notable consequences of this effect is that specific impulse of xenon increases by almost 30% with increasing current density. This can be understood from considering a modified version of the theoretical formulation for specific impulse. This is based on assuming complete electrostatic acceleration of the ions and allowing for a multiply-charged plume: $I_{sp(th)} = \sqrt{2eZ_{avg}V_d/m_i}$, where $Z_{avg} = \Sigma(\Omega_i Z_i)$. This expression captures the fact that as the plasma gains a progressively higher charge state, the specific impulse scales with the average effective charge per unit mass. The practical implication of this result is the apparent increase in fuel efficiency (a consequence of increasing specific impulse) with higher current density. Figure 20 highlights the difference in trends of specific impulse when accounting for only singly-charged ions versus including multiply-charged ions. The trends in Fig. 20b more closely resemble the curves in the anode efficiency as seen in Fig. 10c.

B. Trends in efficiency

We remark in this section on several notable trends and implications from our efficiency results. First, we comment on the fact that Fig. 16 showed maxima with discharge current for both xenon and krypton. This can be explained primarily by the balance of a decreasing beam utilization efficiency against an increasing mass utilization efficiency. As we briefly discussed in the preceding section, the drop in beam utilization suggests physically that electron current confinement suffers with higher current density. This trend has previously been hypothesized in the context of Hall thrusters [14] and indeed is exhibited here by a near monotonic decrease. Notably, we see that the effective slope of the beam utilization with discharge current for both xenon and krypton above 50 A is approximately the same, suggesting that in both cases the loss in confinement scales in approximately the same way within some range of currents.

As we also briefly noted in Sec. V.C, the mass utilization appears to increase and achieve 100% with increasing discharge current. This effect can be explained by the fact that the mean free path for ionization of neutrals in the channel scales as $\lambda_{iz} = (n_i \sigma_{iz})^{-1}$, where n_i is the ion density and σ_{iz} is the ionization cross-section for the gas. For a fixed discharge voltage, the number density of ions/electrons (which are equal due to quasineutrality) is approximately proportional to the discharge current: $n_i \propto I_d$. We thus find that the mean free path for ionization scales as $\lambda_{iz} \propto (I_d \sigma_{iz})^{-1}$. From this relationship, we see that the mean free path for ionization decreases with higher currents and can in principle lead to a state where it is sufficiently small for all inlet gas to be ionized before exiting the channel.

Building on this argument, we see that the mean free path scales with the ionization cross-section for the gas. This cross-section is smaller for krypton than xenon, which in turn may explain why higher plasma densities (and by extension discharge currents) are required for the mass utilization efficiency to reach unity for this gas. This in turn implies that the discharge current of maximum efficiency for a given propellant is in part driven by its ionization cross-section. When convolved with the decreasing beam utilization efficiency, the shift in the transition to 100% mass utilization to a value of higher discharge current for krypton has the effect of pushing the maximum value for overall efficiency of krypton to occur at a higher discharge current than xenon. One other notable effect of this trade is that once the mass utilization has reached 100% efficiency, the beam utilization dominates the overall efficiency curve, leading to an eventual decrease in performance. The more rapid gains in mass utilization can overcome this trend, which—combined with the fact that the beam utilization of krypton only starts decreasing at discharge currents above 50 A—may ultimately explain why krypton efficiencies are able to exceed xenon at higher currents.

As an additional implication of this result, we see that the increase in current density appears to be able to compensate for the traditional losses associated with gases with lower ionization cross-sections. This invites the possibility that operating Hall thrusters at higher current densities may enable more efficient performance on alternative gases. This possibility has been suggested in previous work [68]. For a final remark, we note that while previous work has suggested that loss in beam utilization may be a defining factor prohibiting operating at higher current densities, our results indicate this is not the case. Indeed, although beam utilization does decrease with current density, the performance remained competitive with typical metrics for Hall thrusters reported at lower power.

C. Low oscillation mode

In Fig. 17, we see that the peak-to-peak oscillation strength of the discharge current generally decreases as power increased. This is especially true for xenon, where at currents over 100 A, we see oscillations of $< 6\%$ of the total current. While krypton does not follow an identical trend to xenon, the oscillations still do generally decrease with

increasing current. Indeed, compared to the > 150% oscillations seen on krypton operating at high-voltage conditions [30], all conditions had fairly mild (< 50%) oscillation strengths.

As a possible explanation for this behavior, we note that recent work has suggested that for fixed discharge voltage, thruster stability can improve with higher discharge current; this stems from the fact that the higher local current densities and corresponding high ionization rates help damp the dominant breathing mode in the thruster [66]. Further, this same work showed that decreasing the residence time of neutrals in the anode can also improve stability margin. Given the high thermal fluxes to the thruster walls heating the anode and the resulting high neutral temperatures, this may also be a contributing factor to the relatively low oscillation levels.

As an alternative, correlational observation, we remark that the qualitative trends in current oscillation appear to match the trends in the fraction of singly-charged ions for both propellants seen in Fig. 13. For xenon, the singly-charged ions steadily decrease from 15 to 100 A before leveling out at 125 A. For krypton, the population of singly-charged ions trend downwards less drastically, with minimal change from 15 to 50 A and from 75 to 100 A. These behaviors are also seen in the oscillation strength at the same current values for both propellants. Although this observation is presently purely correlational, further exploration may yield insight into the role of multiply-charged species in the breathing mode.

D. Facility effects at high power density

In addition to examining the operational limits of a Hall thruster at atypically high current densities, our results also help provide exploratory insight into the challenges of Hall thruster ground testing at high power. While the impact of carbon backsputter and facility pressure were already anticipated before this study, we have been able to provide a new dataset of direct measurements for LVTF, a highly capable test facility. There ultimately remain outstanding questions as to how these elevated pressures and sputtered material impact performance, and as a direct result, we recognize that the validity of the measurements we report here may ultimately need to be qualified.

Ongoing efforts under JANUS ultimately must use data such as what we have collected throughout this test campaign to inform strategies for deconvolving or mitigating facility effects in order to improve confidence in the transition of ground measurements like ours to flight [24]. We remark here as well that our results have highlighted some of the more nuanced challenges with high power operation. For example, we have found that standard designs for probes such as RPAs begin to break down under these new operating limits. This invites the question as to how to adapt these tools to be better suited for this new environment.

As a final comment, we remark that while alternative concepts like liquid metal field MPD thrusters do not in principle have the same challenges with facility pressure as gas-fed Hall thrusters, the problem of diagnostic development and backsputter largely remain the same. Indeed, as we show in the next section, our thrust densities are comparable to those expected of applied-field MPDs. We therefore anticipate that these facility effects may also pose a testing challenge for other high-power devices.

E. Implications for Hall thrusters as an option for high power SEP and NEP

We conclude our discussion with a comment on the implications of our results for Hall thrusters as a candidate technology for high power applications. As discussed in the introduction, the traditionally perceived limit to thrust density of Hall thrusters has been a major limitation for scaling to higher power when contrasted with fully electromagnetic concepts like MPD thrusters. Our results serve to show that these traditional scaling laws may ultimately not be absolute. Indeed, we have been to show that efficiency does not precipitously drop with an approximately 7.5–10 times increase in current density compared to the nominal operating condition of our Hall thruster. We were able to achieve this result with moderate specific impulse, which in turn translates to an attractive thrust-to-power ratio.

To put this result in context, we show in Fig. 21a the normalized thrust density of our device for both xenon and krypton compared to thrust densities compiled from Princeton University's Electric Propulsion and Plasmadynamics Laboratory (EPPDyL) online database of applied-field MPD thrusters [69]. In this case, we have used the radius of the solenoid of the AP-MPD for determining thrust density, and we compare this to thrust density using the outer radius of the H9 discharge. All results are normalized to the thrust density of the H9 operating on xenon at 300 V and 15 A. This result shows that H9 MUSCLE at these current densities is not only competitive but can exceed AF-MPD thrust density for this power range. We also show in Fig. 21b the thrust-to-power ratios of the H9 MUSCLE, which also exceed most of the values extracted from the the AF-MPD database. This improvement primarily stems from the fact that the MPDs operate on lower-mass propellants than xenon and krypton, therefore leading to higher specific impulses and lower thrust-to-power ratios.
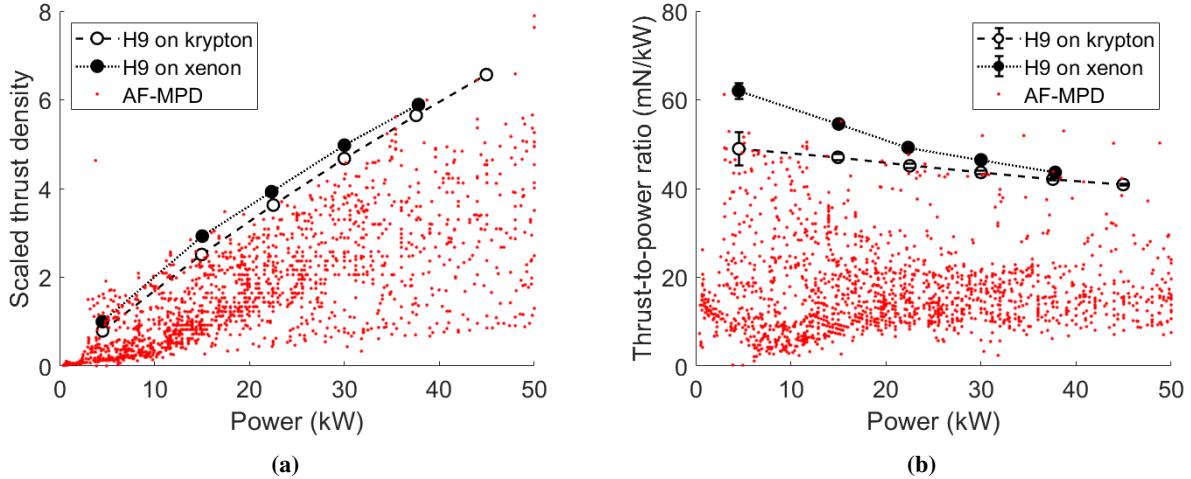
Fig. 21 Comparison of a) thrust densities and b) thrust-to-power ratios of the H9 operating on xenon and krypton compared to a database of AF-MPD measurements [69]. Thrust densities are normalized to that of the H9 operating on xenon at 4.5 kW.

The major implication of this comparison is that over this 15–45 kW power regime, Hall thrusters can in principle offer competitive thrust density scaling compared to other high power concepts. This makes them particularly attractive for mission applications using nuclear architectures [3]. With that said, we caveat this result with the fact that it is unclear how well this scaling holds as the specific power and thrust increase. We may ultimately find, as the trends in our efficiency results suggest (especially the decrease in beam utilization), that performance may decrease to undesirable limits. However, there may ultimately be design decisions that help offset these potential losses, such as increased magnetic field strength.

As a final comment, we emphasize here that this work was fundamental in nature, performed on a laboratory thruster with a controlled, actively cooled system. Our goal was to test the validity of the traditional arguments about electron confinement at higher current. In practice, transitioning this physics-based experiment to flight has many major technical engineering challenges related to thermal limits as well as magnetic field design.

VII. Conclusion

The goal of effort has been to investigate the fundamental limits of current density scaling in a Hall effect thruster. This work has been motivated by the increasing interest in developing high power technologies enabling nuclear architectures for missions like crewed explorations of Mars. In this context, while Hall thrusters are considered a leading candidate technology, one of their primary historically-perceived limitations has been a limit in their achievable thrust density.

Motivated by recent experimental findings and theoretical studies, we investigated in this study the limits of the traditional scaling laws for maximum current density in a Hall thruster. We made modifications to a 9-kW class magnetically shielded laboratory thruster to support this test and systematically characterized the resultant H9 MUSCLE's performance on xenon and krypton from its nominal current of 15 A to a maximum of 150 A. We employed both global performance measurements to characterize thrust, specific impulse, and efficiency, as well as far-field probes to measure the phenomenological efficiency modes of the thruster. Key findings include that

- Performance does decrease at the highest current densities but remains competitive with the performance metrics for conventional Hall thrusters operated at lower powers.
- Krypton performance exceeds xenon performance above a threshold current.
- The plasma state for xenon becomes predominantly doubly-charged with increasing current.
- The mass utilization efficiency reaches 100% for both gases.
- The thruster transitions to a highly quiescent mode on xenon for currents exceeding 100 A.

We have attempted to discuss and explain these trends qualitatively in the context of Hall thruster theory. In parallel, we have used this test to highlight key challenges with testing higher power concepts, quantifying the degree of backsputter

and background pressure and showing the limitations of conventional probing methods on these higher power concepts.

From a practical perspective, our findings may have implications for future research efforts. We have discussed, for example, how operating at higher current density may enable efficient operation on propellants that have lower ionization cross-sections than xenon. We have also shown that over the power range we investigated, the thrust densities and thrust-to-power ratios of the modified Hall thruster can exceed those of a competing technology, the applied-field magnetoplasmadynamic thruster. We caveat both of these possible implications, however, with the remark that it is not certain if these advantages remain at even higher current densities In addition, this study was a laboratory demonstration on a laboratory device, and there remain several potentially major challenges with a more practical flightlike implementation. With that said, this study, which has explored fundamental limits of Hall thruster operation, has shown that this technology may be a key enabler for new and exciting capabilities such as crewed exploration of the solar system.

Appendix A: Probe Correction Factors

A. E×B CEX correction

The CEX correction factors for the E×B traces are calculated as

$$(j/j_0)_i = \exp\left(-n_0 \sigma_i z\right),\tag{16}$$

where n_0 is the background neutral density, σ_i is the cross-sectional area for the ith ion species, and z is the distance of the E×B probe from the exit plane. We calculated n_0 from our measurements of chamber pressure in the exit plane shown in Table 1, with an uncertainty in our ion gauge pressure measurement of 20%. The expressions for the cross-sectional areas of the ith charge state of xenon are taken from Ref. [44] and [30]:

$$\sigma_1|_{Xe} = (87.3 - 13.6 \, \log\left(V_1\right)) \times 10^{-20}\tag{17}$$

$$\sigma_2|_{Xe} = (45.7 - 8.9 \, \log\left(2V_2\right)) \times 10^{-20}\tag{18}$$

$$\sigma_3|_{Xe} = (16.9 - 3.0 \, \log\left(3V_3\right)) \times 10^{-20},\tag{19}$$

where V_i is the voltage through which the ith ion species is accelerated. For our analysis, we assumed that all values of V_i are equivalent to the calculated acceleration voltage V_a.

For krypton, we follow the same methodology in Ref. [30] and use cross-sectional areas from Ref. [45] for the first two charge states:

$$\sigma_1|_{Kr} = (80.7 - 14.7 \, \log\left(V_1\right)) \times 10^{-20}\tag{20}$$

$$\sigma_2|_{Kr} = (44.6 - 9.8 \, \log\left(2V_2\right)) \times 10^{-20},\tag{21}$$

where we once again used the acceleration voltage V_a for each species. We approximate the cross-sectional area of triply-charged krypton using the expression in Eq. 19.

B. Faraday probe geometric and SEE corrections

A correction factor must be applied to the Faraday probe trace to account for the spacing between the guard ring and the collector. This factor is

$$\kappa_G = \pi(R_{GR}^2 - R_C^2)\left(\frac{2\pi R_c h_C}{2\pi R_C h_C + 2\pi R_{GR} h_{GR}}\right),\tag{22}$$

where R_{GR}, R_C, h_{GR}, and h_C are the radii and heights of the guard ring and collector, respectively.

SEE coefficients γ for xenon and krypton are used with the charge fractions determined by the E×B probe to correct for secondary electron emission in the current density trace with the correctional factor κ_{SEE}. The correctional factor is

$$\kappa_{SEE} = \frac{1}{1 + \sum_i \dfrac{\Omega_i \gamma_i}{Z_i}},\tag{23}$$

where γ_i is the SEE coefficient of the ith charge state, and Z_i is the ith charge state from 1 to 3. The SEE coefficients are determined following the methodology outlined in our previous work [30] and are shown in Table 2.

Gas	γ_1	γ_2	γ_3
Xe	0.021	0.199	0.697
Kr	0.069	0.296	0.859

Table 2   Secondary electron emission coefficients for charge states 1 through 3 of xenon and krypton.

Appendix B: Tabulated Thrust and Efficiency Data

Tables 3 and 4 show the values and uncertainties of thrust, specific impulse, anode efficiency, and total efficiency for each condition.

Current (A)	Power (kW)	Thrust (mN)	Isp (s)	η_a (%)	η_{tot} (%)	I_d osc. (%)
15	4.5	280 ±8	1754 ±60	57.1 ±6.0	49.8 ±5.4	69 ±4
50	15	820 ±10	2174 ±32	62.2 ±2.2	57.0 ±2.4	39 ±3
75	22.5	1100 ±10	2244 ±25	58.0 ±1.4	53.4 ±1.8	22 ±3
100	30	1394 ±10	2294 ±20	55.9 ±1.1	51.7 ±1.5	6 ±1
125	37.5	1650 ±10	2309 ±17	52.9 ±0.8	49.0 ±1.3	4 ±1

Table 3 Xenon performance measurements and discharge current oscillations at 300 V.

Current (A)	Power (kW)	Thrust (mN)	Isp (s)	η_a (%)	η_{tot} (%)	I_d osc. (%)
15	4.5	222 ±17	1889 ±149	48.5 ±7.0	42.4 ±6.2	43 ±6
50	15	704 ±11	2184 ±36	53.9 ±2.0	49.3 ±2.1	33 ±2
75	22.5	1016 ±10	2331 ±25	55.2 ±1.4	50.8 ±1.7	24 ±2
100	30	1309 ±9	2465 ±19	56.4 ±1.0	52.1 ±1.5	34 ±2
125	37.5	1582 ±8	2534 ±15	56.0 ±0.8	51.8 ±1.3	32 ±3
150	45	1839 ±10	2567 ±16	55.1 ±0.8	51.1 ±1.3	19 ±1

Table 4 Krypton performance measurements and discharge current oscillations at 300 V.

Tables 5 and 6 show the values and uncertainties of phenomenological efficiencies and anode efficiency calculated from them as inferred from probe measurements for each condition.

Current (A)	Power (kW)	η_b (%)	η_q (%)	η_m (%)	η_v (%)	η_d (%)	$\eta_{a,prod}$ (%)
15	4.5	81.5 ±6.0	97.9 ±3.2	93.4 ±9.4	95.4 ±1.1	85.4 ±2.0	60.8 ±9.9
50	15	77.2 ±8.0	96.9 ±5.4	111.6 ±11.8	95.6 ±2.5	82.3 ±1.6	65.6 ±10.8
75	22.5	75.1 ±1.3	96.3 ±6.8	108.1 ±2.4	96.1 ±1.9	79.4 ±2.5	59.6 ±5.1
100	30	72.6 ±1.5	96.9 ±9.3	98.4 ±2.3	98.1 ±1.5	78.2 ±1.6	53.1 ±5.6
125	37.5	71.2 ±1.8	97.0 ±10.6	102.3 ±2.8	100.7 ±3.8	77.7 ±2.2	55.3 ±7.0

Table 5 Xenon efficiencies from probe measurements at 300 V.

Current (A)	Power (kW)	η_b (%)	η_q (%)	η_m (%)	η_v (%)	η_d (%)	$\eta_{a,prod}$ (%)
15	4.5	70.2 ±5.4	97.8 ±2.6	71.9 ±7.4	95.4 ±1.0	79.0 ±2.1	37.2 ±6.1
50	15	75.7 ±1.8	97.9 ±5.9	94.5 ±3.0	96.7 ±1.6	80.1 ±1.7	54.3 ±4.5
75	22.5	74.9 ±1.5	97.3 ±7.1	98.0 ±2.4	94.9 ±1.9	79.1 ±1.6	53.6 ±4.7
100	30	73.1 ±1.6	97.4 ±8.8	105.6 ±2.5	94.4 ±7.8	79.2 ±2.1	56.3 ±7.4
125	37.5	72.7 ±3.0	97.4 ±10.2	109.1 ±4.6	91.1 ±4.0	79.3 ±1.9	55.8 ±7.3
150	45	71.8 ±1.8	96.9 ±10.7	104.0 ±2.8	95.4 ±2.8	78.1 ±2.5	53.9 ±6.7

Table 6 Krypton efficiencies from probe measurements at 300 V.

Acknowledgments

References

[1] "Space Nuclear Propulsion for Human Mars Exploration," Tech. rep., National Academies of Sciences, Engineering, and Medicine, Washington, DC, 2021.

[2] "Next Space Technologies for Exploration Partnerships Broad Agency Announcement NNH15ZCQ001K," Tech. rep., National Aeronautics and Space Administration, 2014.

[3] Duchek, M. E., Machemer, W., Harnack, C., Clark, M. A., Pensado, A. R., Palomares, K. B., Polzin, K. A., Martin, A., Curran, F., Myers, R., et al., "Key Performance Parameters for MW-Class NEP Elements and their Interfaces," *ASCEND 2022*, 2022, p. 4273.

[4] Jankovsky, R., Tverdokhlebov, S., and Manzella, D., "High power Hall thrusters," *35th Joint Propulsion Conference and Exhibit*, 1999, p. 2949.

[5] Pote, B., Hruby, V., and Monheiser, J., "Performance of an 8 kW Hall thruster," Tech. rep., BUSEK CO INC NATICK MA, 2000.

[6] Kamhawi, H., Haag, T. W., Smith, T., Herman, D., Huang, W., Shastry, R., Peterson, P., and Mathers, A., "Performance Characterization of the Air Force Transformational Satellite 12 kW Hall Thruster," Tech. rep., 2013.

[7] Szabo, J., Pote, B., Hruby, V., Byrne, L., Tadrake, R., Kolencik, G., Kamhawi, H., and Haag, T., "A commercial one Newton Hall effect thruster for high power in-space missions," *47th AIAA/ASME/SAE/ASEE Joint Propulsion Conference & Exhibit*, 2011, p. 6152.

[8] Soulas, G., Haag, T., Herman, D., Huang, W., Kamhawi, H., and Shastry, R., "Performance test results of the NASA-457M v2 Hall thruster," *48th AIAA/ASME/SAE/ASEE Joint Propulsion Conference & Exhibit*, 2012, p. 3940.

[9] Mason, L., Jankovsky, R., and Manzella, D., "1000 hours of testing on a 10 kilowatt Hall effect thruster," *37th Joint Propulsion Conference and Exhibit*, 2001, p. 3773.

[10] Hall, S. J., "Characterization of a 100-kW Class Nested-Channel Hall Thruster," Ph.D. thesis, University of Michigan, Ann Arbor, MI, 2018.

[11] Hall, S. J., Jorns, B. A., Cusson, S. E., Gallimore, A. D., Kamhawi, H., Peterson, P. Y., Haag, T. W., Mackey, J. A., Baird, M. J., and Gilland, J. H., "Performance and high-speed characterization of a 100-kW nested Hall thruster," *Journal of Propulsion and Power*, Vol. 38, No. 1, 2022, pp. 40–50.

[12] Manzella, D. H., *Performance Evaluation of the SPT-140*, Vol. 206301, National Aeronautics and Space Administration, Lewis Research Center, 1997.

[13] Grishin, S. D., Erofeev, V. S., Zharinov, A. V., Naumkin, V. P., and Safronov, I. V., "Characteristics of a Two-Stage Ion Accelerator with an Anode Layer," *Journal of Applied Mechanics and Technical Physics*, Vol. 19, 1978, pp. 166–173.

[14] Dannenmayer, K., and Mazouffre, S., "Elementary scaling relations for hall effect thrusters," *J. Propul. Power*, Vol. 27, No. 1, 2011, pp. 236–245.

[15] Morozov, A. I., and Savelyev, V. V., "Fundamentals of Stationary Plasma Thruster Theory," *Reviews of Plasma Physics*, Vol. 21, 2000, pp. 203–391.

[16] Goebel, D. M., and Katz, I., *Fundamentals of Electric Propulsion: Ion and Hall Thrusters*, Jet Propulsion Laboratory, California Institute of Technology, Pasadena, CA, 2008.

[17] Simmonds, J., Raitses, Y., and Smolyakov, A., "A Theoretical Thrust Density Limit for Hall Thrusters," *Journal of Electric Propulsion*, 2022.

[18] Hall, S. J., Jorns, B., Gallimore, A., and Hofer, R. R., "Expanded Thruster Mass Model Incorporating Nested Hall Thrusters," *53rd AIAA/SAE/ASEE Joint Propulsion Conference*, American Institute of Aeronautics and Astronautics (AIAA), Atlanta, GA, 2017, pp. 2017–4729.

[19] Boeuf, J. P., "Tutorial: Physics and modeling of Hall thrusters," *J. Appl. Phys.*, Vol. 121, No. 1, 2017, p. 011101. https://doi.org/10.1063/1.4972269.

[20] Su, L. L., and Jorns, B. A., "Performance at High Current Densities of a Magnetically-Shielded Hall Thruster," *Propulsion and Energy Forum*, American Institute of Aeronautics and Astronautics, 2021. https://doi.org/10.2514/6.2021-3405.

[21] Diamant, K. D., Liang, R., and Corey, R. L., "The Effect of Background Pressure on SPT-100 Hall Thruster Performance," *50th AIAA/ASME/SAE/ASEE Joint Propulsion Conference*, Cleveland, OH, 2014.

[22] Polk, J. E., Pancotti, A., Haag, T., King, S., Walker, M., Blakely, J., and Ziemer, J., "Recommended practice for thrust measurement in electric propulsion testing," *Journal of Propulsion and Power*, Vol. 33, No. 3, 2017, pp. 539–555.

[23] Williams, G. J., Kamhawi, H., Choi, M., Haag, T. W., Huang, W., Herman, D. A., Gilland, J. H., and Peterson, P. Y., "Wear Trends of the HERMeS Thruster as a Function of Throttle Point," *35th International Electric Propulsion Conference*, Atlanta,

GA, 2019.

[24] Walker, M. L. R., Lev, D., Saeedifard, M., Jorns, B., Foster, J., Gallimore, A. D., Gorodetsky, A., Rovey, J. L., Chew, H. B., Levin, D., Williams, J. D., Yalin, A., Wirz, R., Marian, J., Boyd, I., Hara, K., and Lemmer, K., "Overview of the Joint AdvaNced PropUlsion InStitute (JANUS)," *37th International Electric Propulsion Conference*, Boston, MA, 2022.

[25] Hofer, R. R., Cusson, S. E., Lobbia, R. B., and Gallimore, A. D., "The H9 Magnetically Shielded Hall Thruster," *35th International Electric Propulsion Conference*, Atlanta, GA, 2017.

[26] Cusson, S. E., Hofer, R. R., Lobbia, R., Jorns, B. A., and Gallimore, A. D., "Performance of the H9 Magnetically Shielded Hall Thrusters," *35th International Electric Propulsion Conference*, Atlanta, Georgia, 2017.

[27] Hofer, R. R., Lobbia, R., and Arestie, S., "Performance of a Conducting Wall, Magnetically Shielded Hall Thruster at 3000-s Specific Impulse," 2022.

[28] Mikellides, I. G., Katz, I., Hofer, R. R., and Goebel, D. M., "Magnetic shielding of a laboratory Hall thruster. I. Theory and validation," *J. Appl. Phys.*, Vol. 115, No. 4, 2014, p. 043303. https://doi.org/10.1063/1.4862313.

[29] Hofer, R. R., Goebel, D. M., Mikellides, I. G., and Katz, I., "Magnetic shielding of a laboratory Hall thruster. II. Experiments," *J. Appl. Phys.*, Vol. 115, No. 4, 2014, p. 043304. https://doi.org/10.1063/1.4862314.

[30] Su, L., and Jorns, B., "Performance comparison of a 9-kW magnetically shielded Hall thruster operating on xenon and krypton," *Journal of Applied Physics*, Vol. 130, No. 16, 2021, p. 163306.

[31] Goebel, D. M., Hofer, R. R., Mikellides, I. G., Katz, I., Polk, J. E., and Dotson, B. N., "Conducting wall hall thrusters," *IEEE Transactions on Plasma Science*, Vol. 43, No. 1, 2015, pp. 118–126.

[32] Grimaud, L., and Mazouffre, S., "Conducting wall Hall thrusters in magnetic shielding and standard configurations," *Journal of Applied Physics*, Vol. 122, No. 3, 2017, p. 033305.

[33] Viges, E. A., Jorns, B. A., Gallimore, A. D., and Sheehan, J. P., "University of Michigan's Upgraded Large Vacuum Test Facility," *36th International Electric Propulsion Conference*, Vienna, Austria, 2019.

[34] Dankanich, J. W., Walker, M., Swiatek, M. W., and Yim, J. T., "Recommended practice for pressure measurement and calculation of effective pumping speed in electric propulsion testing," *J. Propul. Power*, Vol. 33, No. 3, 2017, pp. 668–680. https://doi.org/10.2514/1.B35478.

[35] Frieman, J. D., Liu, T. M., and Walker, M. L. R., "Background Flow Model of Hall Thruster Neutral Ingestion," *Journal of Propulsion and Power*, Vol. 33, No. 5, 2017, pp. 1087–1101. https://doi.org/10.2514/1.b36269.

[36] Hofer, R. R., and Gallimore, A. D., "Efficiency analysis of a high-specific impulse Hall thruster," *40th Joint Propulsion Conference*, American Institute of Aeronautics and Astronautics, Ft. Lauderdale, FL, 2004.

[37] Hofer, R., Katz, I., Goebel, D., Jameson, K., Sullivan, R., Johnson, L., and Mikellides, I., "Efficacy of Electron Mobility Models in Hybrid-PIC Hall Thruster Simulations," *44th Joint Propulsion Conference and Exhibit*, American Institute of Aeronautics and Astronautics, Hartford, CT, 2008. https://doi.org/10.2514/6.2008-4924.

[38] Hofer, R. R., "Development and Characterization of High-Efficiency, High-Specific Impulse Xenon Hall Thrusters," Ph.D. thesis, University of Michigan, 2004.

[39] Efron, B., and Tibshirani, R. J., CRC Press, 1994.

[40] Lobbia, R. B., and Beal, B. E., "Recommended Practice for Use of Langmuir Probes in Electric Propulsion Testing," *J. Propul. Power*, Vol. 33, No. 3, 2017, pp. 566–581. https://doi.org/10.2514/1.B35531.

[41] Huang, W., Shastry, R., Soulas, G. C., and Kamhawi, H., "Farfield Plume Measurement and Analysis on the NASA-300M and NASA-300MS," *33rd International Electric Propulsion Conference*, Washington D.C., USA, 2013.

[42] Shastry, R., Hofer, R. R., Reid, B. M., and Gallimore, A. D., "Method for analyzing E×B probe spectra from Hall thruster plumes," *Rev. Sci. Instrum.*, Vol. 80, No. 6, 2009, p. 063502. https://doi.org/10.1063/1.3152218.

[43] Huang, W., and Shastry, R., "Analysis of Wien filter spectra from Hall thruster plumes," *Rev. Sci. Instrum.*, Vol. 86, No. 7, 2015, p. 073502. https://doi.org/10.1063/1.4923282.

[44] Miller, J. S., Pullins, S. H., Levandier, D. J., Chiu, Y. H., and Dressler, R. A., "Xenon charge exchange cross sections for electrostatic thruster models," *J. Appl. Phys.*, Vol. 91, No. 3, 2002, pp. 984–991. https://doi.org/10.1063/1.1426246.

[45] Hause, M. L., Prince, B. D., and Bemish, R. J., "Krypton charge exchange cross sections for Hall effect thruster models," *J. Appl. Phys.*, Vol. 113, No. 16, 2013, p. 16330. https://doi.org/10.1063/1.4802432.

[46] Brown, D. L., Walker, M. L., Szabo, J., Huang, W., and Foster, J. E., "Recommended practice for use of Faraday probes in electric propulsion testing," *J. Propul. Power*, Vol. 33, No. 3, 2017, pp. 582–613.

[47] Hofer, R. R., and Gallimore, A. D., "Recent Results from Internal and Very-Near-Field Plasma Diagnostics of a High Specific Impulse Hall Thruster," *28th International Electric Propulsion Conference*, Toulouse, France, 2003.

[48] Lu, C.-S., and Lewis, O., "Investigation of film-thickness determination by oscillating quartz resonators with large mass load," *Journal of Applied Physics*, Vol. 43, No. 11, 1972, pp. 4385–4390.

[49] Bugrova, A. I., Bishaev, A. M., Desyatskov, A. V., Kozintseva, M. V., Lipatov, A. S., and Dudeck, M., "Experimental investigations of a krypton stationary plasma thruster," *Int. J. Aerosp. Eng.*, 2013, p. 686132. https://doi.org/10.1155/2013/686132.

[50] Kurzyna, J., Jakubczak, M., Szelecka, A., and Dannenmayer, K., "Performance tests of IPPLM's krypton Hall thruster," *Laser Part. Beams*, Vol. 36, No. 1, 2018, pp. 105–114. https://doi.org/10.1017/S0263034618000046.

[51] Hofer, R. R., Peterson, P. Y., Jacobson, D. T., and Manzella, D. M., "Factors Affecting the Efficiency of Krypton Hall Thrusters," *46th Meeting of the APS Division of Plasma Physics*, Savannah, GA, 2004.

[52] Linnell, J. A., and Gallimore, A. D., "Efficiency Analysis of a Hall Thruster Operating with Krypton and Xenon," *J. Propul. Power*, Vol. 22, No. 6, 2006, pp. 1402–1418.

[53] Kamhawi, H., Haag, T., Jacobson, D., and Manzella, D., "Performance Evaluation of the NASA-300M 20 kW Hall Thruster," *47th Joint Propulsion Conference and Exhibit*, American Institute of Aeronautics and Astronautics, San Diego, CA, 2011.

[54] Peterson, P., Jacobson, D., Manzella, D., and John, J., "The Performance and Wear Characterization of a High-Power High-Isp NASA Hall Thruster," *41st Joint Propulsion Conference and Exhibit*, American Institute of Aeronautics and Astronautics, Tucson, AZ, 2005. https://doi.org/10.2514/6.2005-4243.

[55] Marrese, C., Gallimore, A. D., Haas, J., Foster, J., King, B., Kim, S. W., and Khartov, S., "An investigation of stationary plasma thruster performance with krypton propellant," *31st Joint Propulsion Conference and Exhibit*, American Institute of Aeronautics and Astronautics, 1995. https://doi.org/10.2514/6.1995-2932.

[56] Jacobson, D. T., and Manzella, D. H., "50 kW Class Krypton Hall Thruster Performance," *39th Joint Propulsion Conference and Exhibit*, NASA, Huntsville, Alabama, 2003.

[57] Jorns, B. A., and Byrne, M. P., "Model for the dependence of cathode voltage in a Hall thruster on facility pressure," *Plasma Sources Science and Technology*, Vol. 30, No. 1, 2021.

[58] Cusson, S. E., Dale, E. T., Jorns, B. A., and Gallimore, A. D., "Acceleration region dynamics in a magnetically shielded Hall thruster," *Phys. Plasmas*, Vol. 26, No. 2, 2019, p. 023506. https://doi.org/10.1063/1.5079414.

[59] Kim, V., "Main physical features and processes determining the performance of stationary plasma thrusters," *Journal of propulsion and power*, Vol. 14, No. 5, 1998, pp. 736–743.

[60] Hofer, R. R., and Gallimore, A. D., "High-specific impulse Hall thrusters, part 2: efficiency analysis," *Journal of Propulsion and Power*, Vol. 22, No. 4, 2006, pp. 732–740.

[61] Brown, D. L., Larson, C. W., Beal, B. E., and Gallimore, A. D., "Methodology and Historical Perspective of a Hall Thruster Efficiency Analysis," *J. Propul. Power*, Vol. 25, No. 6, 2009, pp. 1163–1177. https://doi.org/10.2514/1.38092.

[62] Reid, B. M., "The influence of neutral flow rate in the operation of Hall thrusters," Ph.D. thesis, University of Michigan, 2009.

[63] Huang, W., Kamhawi, H., and Haag, T., "Facility Effect Characterization Test of NASA's HERMeS Hall Thruster," *52nd Joint Propulsion Conference*, Salt Lake City, UT, 2016. https://doi.org/10.2514/6.2016-4828.

[64] Karadag, B., Cho, S., and Funaki, I., "Thrust performance, propellant ionization, and thruster erosion of an external discharge plasma thruster," *Journal of Applied Physics*, Vol. 123, No. 15, 2018, p. 153302.

[65] Jameson, K. K., Goebel, D. M., Hofer, R. R., and Watkins, R. M., "Cathode coupling in Hall thrusters," *30th International Electric Propulsion Conference*, 2007, pp. 2007–278.

[66] Jorns, B. A., Byrne, M., Roberts, P., Su, L., Dale, E., and Hofer, R. R., "Prediction and Mitigation of the Mode Transition in a Magnetically Shielded Hall Thruster at High-Specific Impulse and Low Power," *37th International Electric Propulsion Conference*, Boston, MA, 2022.

[67] Randolph, T., Bekrev, M., Day, M., Fischer, G., Koriakin, A., Kozubsky, K., Krochak, L., Maslennikov, N., Pidgeon, D., Pridannikov, S., Rogers, W., Staley, M., and Yuriev, A., "Integrated Test of an SPT-100 Subsystem," *33rd Joint Propulsion Conference and Exhibit*, Seattle, WA, 1997.

[68] Marchioni, F., and Cappelli, M. A., "Extended channel Hall thruster for air-breathing electric propulsion," *Journal of Applied Physics*, Vol. 130, No. 5, 2021, p. 053306.

[69] Electric Propulsion and Plasma Dynamics Laboratory, "AF-MPD Thruster Database," , 2022. URL https://alfven.princeton.edu/tools/afmpdt-database/.